13352 *Biochemistry* **2007,** *46,* 13352−13369

The Reaction Mechanism of Paraoxon Hydrolysis by Phosphotriesterase from Combined QM/MM Simulations†

Kin-Yiu Wong and Jiali Gao*

Department of Chemistry and Minnesota Supercomputing Institute, University of Minnesota, Smith Hall, 207 Pleasant Street SE, Minneapolis, Minnesota 55455

Received March 7, 2007; Revised Manuscript Received July 31, 2007

ABSTRACT: Molecular dynamics simulations employing combined quantum mechanical and molecular mechanical (QM/MM) potentials have been carried out to investigate the reaction mechanism of the hydrolysis of paraoxon by phosphotriesterase (PTE). We used a dual-level QM/MM approach that synthesizes accurate results from high-level electronic structure calculations with computational efficiency of semiempirical QM/MM potentials for free energy simulations. In particular, the intrinsic (gas-phase) energies of the active site in the QM region are determined by using density functional theory (B3LYP) and second-order Møller-Plesset perturbation theory (MP2) and the molecular dynamics free energy simulations are performed by using the mixed AM1:CHARMM potential. The simulation results suggest a revised mechanism for the phosphotriester hydrolysis mechanism by PTE. The reaction free energy profile is mirrored by structural motions of the binuclear metal center in the active site. The two zinc ions occupy a compact conformation with an average zinc−zinc distance of 3.5 ± 0.1 Å in the Michaelis complex, whereas it is elongated to 5.3 ± 0.3 Å at the transition state and product state. The substrate is loosely bound to the more exposed zinc ion (Zn_β^{2+}) at an average distance of 3.8 Å ± 0.3 Å. The P═O bond of the substrate paraoxon is activated by adopting a tight coordination to the Zn_β^{2+}, releasing the coordinate to the bridging hydroxide ion and increasing its nucleophilicity. It was also found that a water molecule enters into the binding pocket of the loosely bound binuclear center, originally occupied by the nucleophilic hydroxide ion. We suggest that the proton of this water molecule is taken up by His254 at low pH or released to the solvent at high pH, resulting in a hydroxide ion that pulls the Zn_β^{2+} ion closer to form the compact configuration and restores the resting state of the enzyme.

Organophosphorus compounds are extensively used as pesticides and insecticides which can accumulate in soil and aquatic organisms under conditions of low temperature, high acidity, and reduced natural light (*1*, *2*). These species are structurally related to compounds used as chemical warfare agents, such as sarin, soman, and VX, which affect the nervous system by covalently inhibiting acetylcholinesterase (*1*, *3*). Therefore, there is great interest in developing bioremediation technologies to facilitate the degradation of organophosphate contaminants including the disposal of chemical weapons. Phosphotriesterase (PTE) catalyzes the hydrolysis of a wide range of phosphoesters (for paraoxon, $k_{cat} \approx 2400$ s^{-1} and $k_{cat}/K_M \approx 3 \times 10^7$M^{-1} s^{-1}) (*1*, *4*). The enzyme PTE is particularly attractive as a biocatalyst because a large number of phosphotriesters can be hydrolyzed, and the enzyme has been immobilized covalently on a number of carriers, including macroporous glasses, nylon, cryogels, and fabric materials (*5*−*7*). There have been considerable experimental and theoretical studies of PTE enzymatic activity (*1*, *4*−*18*). Nevertheless, the enzyme mechanism is still not fully understood especially on the nature of the bimetallic zinc center in the active site. In this work, we employ molecular dynamics (MD[1]) simulations and combined quantum mechanical and molecular mechanical (QM/MM) methods (*19*, *20*) to examine the catalytic mechanism of PTE in paraoxon hydrolysis.

The three-dimensional structures of PTE with and without substrate-analogue inhibitors have been determined by X-ray crystallographic diffraction (*21*, *22*). The enzyme consists of a homodimer of 329 amino acids in each monomer, related by a C_2 symmetry. The monomer folds into an $(\alpha\beta)_8$-barrel motif, with two additional antiparallel β-strands at the amino terminus. The active site is positioned at the carboxyl-terminal end of the central β-sheet core, and it contains a binuclear metal center, in which two zinc cations are bound within a cluster of four histidine residues (Figure 1). One of the divalent cations, Zn_α^{2+} (Figure 1), is coordinated to two

---

† This work has been supported by the National Institutes of Health and by the Army Research Laboratory through the Army High-Performance Computing Research Center (AHPCRC) under the auspices of the Department of the Army, Army Research Laboratory DAAD 19-01-2-0014.

* Author to whom correspondence should be addressed. E-mail: gao@chem.umn.edu. Phone: 612-625-0769. Fax: 612-626-7541.

[1] Abbreviations: AM1, Austin model 1; AMBER, assisted model building with energy refinement; B3LYP, Becke-3−Lee−Yang−Parr density functional; CHARMM, chemistry at Harvard macromolecular mechanics; DFT, density functional theory; DL, dual-level; GHO, generalized hybrid orbital; HL, high-level; LL, low-level; MD, molecular dynamics; MEP, minimum energy reaction path; MM, molecular mechanics; PDB, protein data bank; PMF, potential of mean force; PTE, phosphotriesterase; QM, quantum mechanics; MP2, second-order Møller−Plesset perturbation theory; SBMD, stochastic boundary molecular dynamics; TST, transition state theory.

10.1021/bi700460c CCC: $37.00

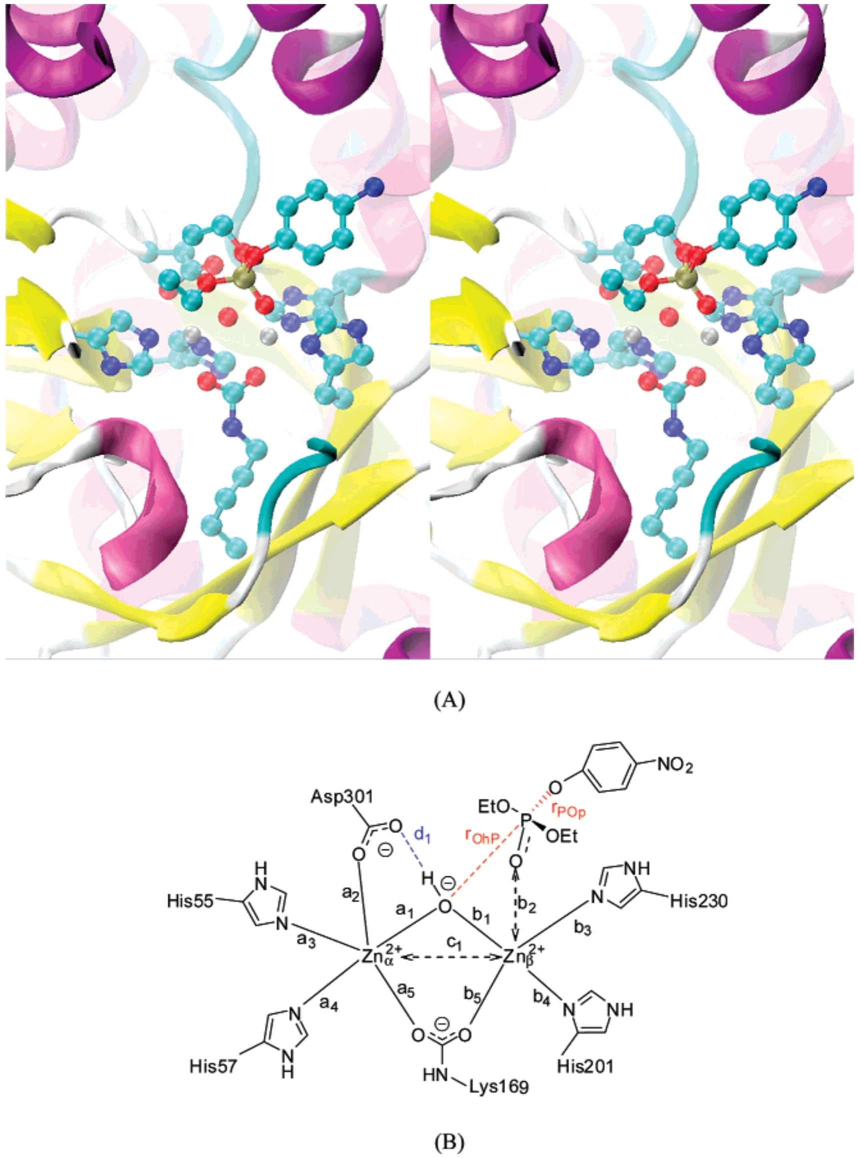

FIGURE 1: Key interactions of the Michaelis complex of paraoxon substrate and phosphotriesterase. The structure is taken from the last configuration of the molecular dynamics simulations of the Michaelis complex state during the umbrella sampling calculations. (A) The QM subsystem (109 atoms) is displayed in a ball-and-stick representation without hydrogen atoms and the nitro group of paraoxon for clarity. The color codes are carbon in cyan, nitrogen in blue, oxygen in red, phosphorus in tan, and zinc in silver. (B) Schematic illustration for clarity of discussion and notations in the text.

histidine residues (His55 and His57) and an aspartic acid residue (Asp301). The second divalent cation, Zn_β^{2+} (Figure 1), is bound to two other histidines (His201 and His230). Zn_α^{2+} is buried in the binding site, whereas Zn_β^{2+} is exposed to the solvent when the substrate is absent. In addition, the two metal ions are bridged by a hydroxide ion (or a water molecule), and by a carbamylate functional group, formed from post-translational carboxylation of Lys169. The binuclear metal center, bridged by a carboxylate group, has been found in the active sites of a number of enzymes that cleave phosphate esters such as in cAMP esterases. It encompasses a growing family of enzymes that employ a similar construct (*23*, *24*). Experimentally, it was found that the zinc metals can be replaced with a variety of other divalent cations without significant loss of enzymatic activity (e.g., cadmium and manganese) (*4*, *18*). Thus, it is of particular interest to understand the nature of the metal centers in catalysis.

Scheme 1: Hydrolysis of Paraoxon

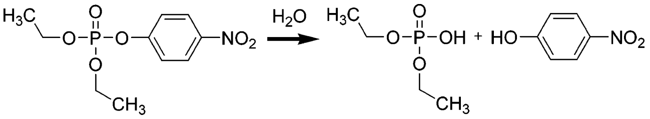

The substrate specificity of PTE is rather broad; the best substrate identified so far is paraoxon (Scheme 1) (*4*, *18*, *25*). The Brønsted plots of the enzymatic kinetic parameters for a series of substituted phenyl ester leaving groups are nonlinear, suggesting a change in rate-limiting step (*18*, *25*). For substrates with a leaving group pK_a greater than 7, the chemical step of phosphate P−O bond cleavage is rate-limiting and shows a typical Brønsted plot, whereas those of pK_a < 7 are likely limited by product release and the rate constants are independent of leaving group pK_a (*25*, *26*). The leaving group of paraoxon has a pK_a of 7.1, lying right at the intersecting point in the Brønsted plot (*25*). The stereoselectivity of PTE is also of interest, which has been subjected to several studies (*27*, *28*). PTE prefers an enantiomer in which the largest group is in the pro-*S* position and the smallest group is in the pro-*R* position (*1*, *11*, *28*).

On the theoretical side, several groups have applied molecular dynamics (MD) simulations and quantum chemical calculations to explore various properties of PTE (*8−17*). These studies were carried out either for the stable species in MD simulations, or for model reactions constructed as clusters mimicking the enzyme active site using electronic structure methods. Useful insights have been obtained into the dynamics of the enzyme and the intrinsic reactivity of the hydrolysis steps. For example, ab initio molecular orbital calculations were carried out to show that the hydrolysis of paraoxon occurs by a concerted process (*15*), which is consistent with the conclusion based on kinetic studies (*29*). Moreover, the computed structures from either density functional theory using B3LYP/6-31G(d) level (*30−32*) on a active site model or MD simulations on the solvated PTE-substrate complex show that a hydroxide ion coordinates to both zinc ions, while a water molecule coordinates only to one zinc ion (*13*). Thus, the computational results provide ample evidence that the identity of the bridging ligand is a hydroxide ion. Additionally, the role of substrate orientation and the flexibility of amino acids in catalysis are also examined by MD simulations (*11*). In these calculations, the opening for the "leaving-group" pocket depends on the substrate and may range from 11 to 18 Å. Nevertheless, the free energy profile has not been obtained and the effects of protein dynamics have not been incorporated into the mechanistic model.

In this study, we propose a revised mechanism for the hydrolysis of paraoxon by PTE. A main feature in the mechanism is the absence of a phosphodiester bridge to both zinc ions as the product intermediate, which is accompanied by the change of the distance between the two zinc ions along the reaction pathway of the formally S_N2 displacement (*18*). Similar structural variations of metal ions have been observed in the hydride transfer reaction catalyzed by xylose isomerase, although unlike the latter case, the changes in metal separation during the reaction catalyzed by PTE and reactions in the amidohydrolase superfamily have not been determined by X-ray crystallography. It would be interesting to investigate experimentally the dynamics of phosphotriesterase and the structural changes during the enzyme reaction.

1. THEORETICAL BACKGROUND AND COMPUTATIONAL DETAILS

Molecular dynamics (MD) simulations using combined quantum mechanical and molecular mechanical (QM/MM) potentials (*19*, *20*, *33−38*) have been carried out in the present study. Below, we describe a dual-level computational procedure (*39−41*), which synthesizes results from high-level electronic structure calculations with computational efficiency for enzyme configurational samplings.

A. Dual-Level QM/MM Potential Energy Surface. We used a combined QM/MM method (*20*, *33−36*) to construct the potential energy surface for the hydrolysis reaction of paraoxon by PTE. The active site (Figure 1), which consists of His55, His57, Lys169, His201, His230, Asp301, the bridging hydroxide anion, two zinc cations, and a paraoxon (a total of 109 atoms), was treated by the semiempirical AM1 model (*42−44*) during MD simulations. The generalized hybrid orbital (GHO) method (*45*, *46*) was employed to couple the QM region with the MM region through six atoms, which are the C_α atoms of residues His55, His57, Lys169, His201, His230, and Asp301. We used the CHARMM22 all-atom empirical force field (*47*) and the three-point-charge TIP3P model (*48*) to represent the rest of the protein and water molecules, respectively. Hereafter, this combined QM/MM potential is denoted as AM1:MM22.

In general, ab initio molecular orbital theory(*49*) or density functional theory (DFT) (*50*) would be ideal for electronic structure calculations, but these methods are still too time-consuming, limiting applications to small systems (*51*) or simplified active site models (*52*), and short simulations for enzyme systems (*52*). Yet, it is essential to carry out free energy simulations to obtain the potential of mean force to study enzyme mechanisms (*19*, *37*, *38*). Consequently, semiempirical models (*42−44*, *53*, *54*) provide a practical approach for performing MD simulations on-the-fly using combined QM/MM potentials (*19*, *55*). However, it is often necessary to correct the energies of the semiempirical model employed (*19*). Here, we use a dual-level procedure in free energy simulations with a semiempirical AM1-QM/MM potential to achieve high-level accuracy for studying enzymatic reactions.

In the dual-level method (*39−41*), we use the combined AM1:MM22 potential to sample enzyme configurations, and then, we use an ab initio method to correct the energies of the AM1 model. Thus, these two aspects are justified separately: (a) Since the AM1:MM22 potential was used in configuration sampling, the structures of this model ought be in agreement with high-level results. (b) Because AM1 energies are replaced by "higher-level" results from ab initio calculations, the "high-level" energies for a large QM subsystem (109 atom system) should be justified in comparison with even higher levels of theory or experiment. We chose the AM1 method because the equilibrium structure of the active site of PTE was found to be in good accord with X-ray crystal structures (*21*) and in good agreement with previous MD studies using the AMBER force field (Supporting Information) (*11*, *12*). We have also examined the PM3 method (*53*), but each zinc ion was tetracoordinated, in contrast to the pentacoordination observed in the X-ray crystal structure and either MD simulations using the AMBER force field or quantum chemical calculations (*13*). Although energies for zinc and phosphorus compounds from semiempirical models can have significant errors (*56*, *57*), they are replaced by ab initio results at the MP2 level (see below). Thus, the use of the combined AM1:MM22 potential is mainly for configurational sampling of a reactive system.

The present dual-level approach combines the efficiency of semiempirical QM/MM simulations with the accuracy of high-level ab initio MO and DFT calculations (*39−41*, *58−63*). The approach is akin to the ONIOM model developed by Morokuma and co-workers (*64*, *65*). The dual-level approach has been used in previous QM/MM simulations (*40*, *41*, *59−62*). In particular, the total energy is partitioned into three terms (*41*):

$$E_{\mathrm{tot}} = \langle \Psi^{\mathrm{o}}_{\mathrm{QM}} | \hat{H}^{\mathrm{o}}_{\mathrm{QM}} | \Psi^{\mathrm{o}}_{\mathrm{QM}} \rangle + [\langle \Psi_{\mathrm{QM}} | \hat{H}^{\mathrm{o}}_{\mathrm{QM}} + \hat{H}_{\mathrm{QM/MM}} | \Psi_{\mathrm{QM}} \rangle - \langle \Psi^{\mathrm{o}}_{\mathrm{QM}} | \hat{H}^{\mathrm{o}}_{\mathrm{QM}} | \Psi^{\mathrm{o}}_{\mathrm{QM}} \rangle] + E_{\mathrm{MM}} \quad (1)$$

where $\hat{H}^{o}_{QM}$ and $\hat{H}_{QM/MM}$ are the Hamiltonians of the QM subsystem and the interactions between the QM and MM regions, respectively, Ψ^{o}_{QM} and Ψ_{QM} are the wavefunctions associated with $\hat{H}^{o}_{QM}$ and $[\hat{H}^{o}_{QM} + \hat{H}_{QM/MM}]$, and E_{MM} is the energy of the MM region. Equation 1 is simplified as follows:

$$E_{tot} = E^{gas}_{QM} + \Delta E_{QM/MM} + E_{MM} \qquad (2)$$

where the first term is the energy of the QM subsystem in the gas phase, and the second term is the interaction energy between the QM and MM regions, corresponding to the energy change of transferring the QM subsystem from the gas phase into the condensed-phase (*35*).

Equation 2 is especially useful in that the total energy of a hybrid QM and MM system is separated into two “independent” terms—the gas-phase energy and the interaction energy—which can now be evaluated using different QM methods. Noticing that the deficiency in semiempirical QM/MM methods is mainly due to a lack of accuracy in the first term of eq 2, we substitute a high level (HL) theory for that term ($E^{gas}_{QM} = E^{HL}_{QM}$). Then, we use the lower level (LL) AM1:MM22 model to determine the interaction energies ($\Delta E_{QM/MM} = \Delta E^{LL}_{QM/MM}$). The latter has been validated through extensive studies of a variety of properties and molecular systems, including computations of free energies of solvation and polarization energies of organic compounds (*35*, *66*, *67*), the free energy profiles for organic reactions (*68*−*70*), and the effects of solvation on molecular structures and on electronic transitions (*69*, *71*). By this substitution, we can obtain a highly accurate dual-level (DL) total energy for the enzyme reaction:

$$E^{DL}_{tot} = E^{HL}_{QM} + \Delta E^{LL}_{QM/MM} + E_{MM} \qquad (3)$$

In the present study, the HL energies are determined by using the B3LYP hybrid density functional theory (*30*−*32*) and the second-order Møller-Plesset perturbation theory (MP2) (*49*), and their performance was validated against previous ab initio studies (*12*−*15*, *17*). Cramer and co-workers showed that the computed activation enthalpies at the MP2/6-31+G(d)//DFT/MIDI! level for the alkaline hydrolysis of sarin are in excellent agreement with experimental results (*17*). In that work, five different density functionals were tested, including the hybrid B3LYP functional. Adopting their approach, we used a mixture of the 6-31G+(d,p) basis (*49*) for the oxygen atom attached to the nitrophenyl group, the phosphorus atom, and the hydroxide anion, the 6-31G(d) basis for the three remaining oxygen atoms of the phosphate group and the two zinc ions, and the MIDI! basis (*72*) for the rest of atoms in the active site. For the MP2 calculations, we have replaced the MIDI! basis by the 6-31G(d) basis set, and compared our results with those for a series of model phosphotriester hydrolysis reactions examined by Zhan and co-workers at the MP2/6-31+G(d) level, who have used a number of other QM methods (*15*). The agreement between our approach and Zhan’s reported work is good with an average error of less than 1 kcal/mol. We used a mixed basis set because the size of the QM subsystem (109 atoms) is still large for multiple reaction path calculations. The comparison with previous full MP2/6-31+G(d) results (*12*−*15*) indicates that the use of this mixed basis function is reasonable. Additional studies were made for the model compound of the product complex. Further details are given as Supporting Information. In the following discussion, we simply denote B3LYP and MP2 calculations without further specifying the details of the basis sets. All ab initio and DFT calculations were carried out with the software package Gaussian 03 (*73*), whereas all calculations at the AM1:MM22 level were performed using the CHARMM (version c32a1) program (*74*).

B. Potential of Mean Force. The free energy of activation for the nucleophilic substitution of paraoxon by a hydroxide ion in phosphotriesterase is obtained by computing the potential of mean force (PMF) (*75*−*77*), $W(z)$, along the reaction coordinate z, which is defined as the difference between the distances of the breaking and forming bonds (Figure 1) (*38*):

$$z = r_{POp} - r_{OhP} \qquad (4)$$

where r_{POp} and r_{OhP} are the distance of the leaving group *p*-nitrophenyl oxygen and the distance of the nucleophile hydroxide oxygen from the phosphorus atom respectively. The PMF is obtained from molecular dynamics simulations by using umbrella sampling (*78*) at temperature T:

$$W(z) = -RT \ln \rho(z) + W_o \qquad (5)$$

where R is the gas constant, W_o is a normalization constant, and $\rho(z)$ is the probability density of finding the system at the reaction coordinate value z (*79*). The value of z at the highest $W(z)$ is called $z^{\ddagger}$, and the TST free energy of activation $\Delta G^{\ddagger}$ is obtained as

$$\Delta G^{\ddagger} = W(z^{\ddagger}) - W(z_R) - G_{R,F} \qquad (6)$$

Here, z_R specifies the reaction coordinate at the reactant state, and $G_{R,F}$ is the classical free energy of the internal degree of freedom that correlates with the reaction coordinate z (*80*).

Using the dual-level (DL) potential energy surface (eq 3), the PMF can be expressed as follows (see also Appendix):

$$W^{DL}(z) = W^{LL}(z) + [E^{HL}_{QM}(z^{MEP}_{LL}) - E^{LL}_{QM}(z^{MEP}_{LL})] + \Delta W^{0} \qquad (7)$$

where $W^{DL}(z)$ is the dual-level PMF, and $W^{LL}(z)$ is the lower-level PMF, determined by using the AM1:MM22 potential (eq 5). The reaction coordinate z^{MEP}_{LL} emphasizes that the correction term (in square brackets) is made along the minimum energy reaction path at the lower-level of theory, and ΔW^{0} is the energy difference between high and lower levels of theory at the reactant state (a constant value accounting for the difference in absolute electronic energies).

An important feature, as shown in the Appendix, is that the high-level correction to the lower-level potential of mean force only needs to be made by computing the potential energy difference between the HL and LL theory along the minimum energy path in the enzyme obtained from the latter potential. Thus, the free energy profile determined using a semiempirical combined QM model can be improved by a small number of high-level energy calculations to achieve the desired accuracy for enzymatic reactions. Indeed, refinements of semiempirical QM/MM simulations have been applied to condensed phase reactions (*39*−*41*, *61*) and to

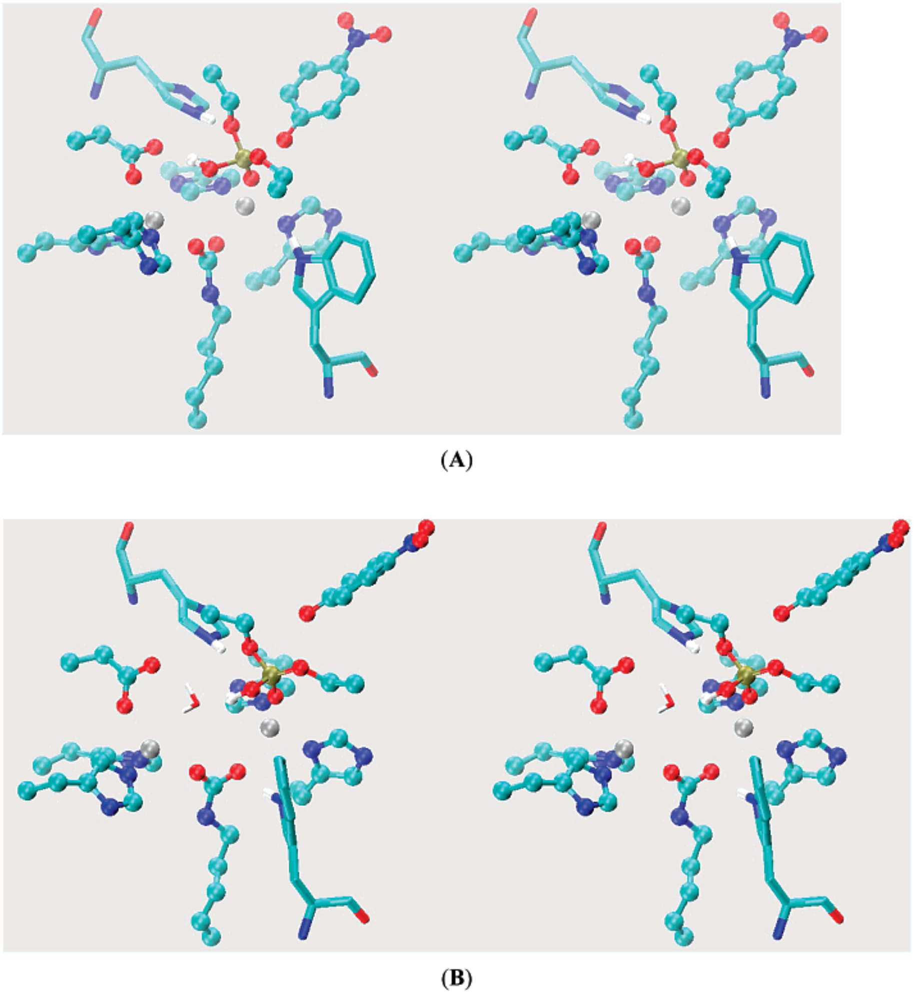

FIGURE 2: Stereoview of the active site configuration from a snapshot of the transition state ensemble (A) and the product−enzyme complex (B) obtained from umbrella sampling simulations for the phosphotriesterase catalyzed hydrolysis reaction. The transition state structure was taken from the simulation at $z = 0.28$ Å, in which the 109 QM atoms are displayed in ball-and-stick. His254 and Trp131 are displayed in thick sticks. The product complex was from the simulation window at $z = 1.4$ Å, in which a water molecule enters the binding site between the two zinc ions. All hydrogen atoms are omitted for clarity except the hydroxide anion, His254, Trp131, and the water molecule. The color scheme is the same as that in Figure 1.

enzymatic reactions, including the work by Martin et al. for the acetohydroxy acid isomeroreductase reaction (*59*), and by Marti et al. (*61*, *62*). Of course, the approach of Morokuma and co-workers, which is similar in spirit by addition and subtraction of energy terms obtained from different levels of theory, has been applied to numerous large molecular systems (*64*).

In the present study of the paraoxon hydrolysis by PTE, we performed umbrella sampling through a total of 22 separate simulations, spanning the entire reaction coordinate, each of which was equilibrated for at least 20 ps followed by an additional 100 ps of configurational sampling. Overall, a total of 6.6 ns of molecular dynamics simulations were performed using the low-level combined AM1:MM22 potential, which was then corrected by B3LYP and MP2 results in the dual-level approximation. The MEP was determined by optimizing the structure of the solvated enzyme−substrate complex as a function of the reaction coordinate, *z*, at the AM1:MM22 level. The starting geometry for the optimizations is from the final configuration in the 100 ps equilibration. Atoms that are 10 Å away from the phosphorus atom were kept frozen, and the total energy of the system was minimized with step size 0.01 Å using the adopted basis Newton−Raphson method (*74*) until the gradient change was less than 0.01 kcal mol^{-1} Å^{-1}. In Figure 2, we illustrate two stereoviews of a snapshot of the last configurations corresponding to the transition state (Figure 2A) and the product state (Figure 2B). To help identifying atoms and interatomic distances in the discussion and in tables, a schematic diagram is depicted in Figure 3.

Since the high-level B3LYP correction term $\Delta W_{\text{QM}}^{\text{HL}}(z)$ was determined along the minimum energy path (MEP) obtained using the AM1:MM22 potential $E_{\text{QM}}^{\text{LL}}$ ($z_{\text{LL}}^{\text{MEP}}$), the deviation between the optimal structures of different levels of theory can lead to non-smooth energy profile at the high-level method. For example, as *z* changes from −0.32 to −0.31 Å, the distance between the bridging hydroxide oxygen and the β-zinc ion (OH:O−Zn_β) changes from 2.48 to 3.27 Å using the AM1:MM22 optimization. Although the AM1 energy only has a small variation, the B3LYP energy changes by 5 kcal/mol. To make the potential smooth, we performed partial geometry optimizations for $z = -0.33$ and −0.32 Å with OH:O−Zn_β fixed at 3.27 Å and for $z = -0.31$, −0.30, −0.29, and −0.28 Å with OH:O−Zn_β fixed at 2.48 Å. Then, we used a linearly scaled average to smooth out the high-level potential at *z* values of about −0.32 Å. The

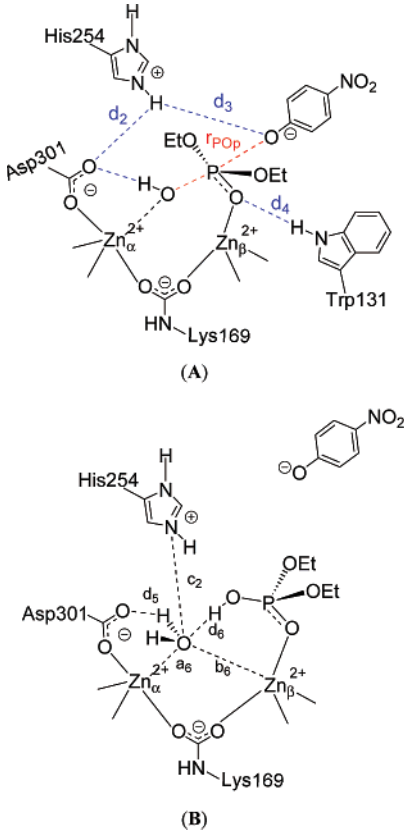

(A)

(B)

Figure 3: Schematic illustration for the transition state (A) and product−enzyme complex (B) that are shown in Figure 2, along with labels for interatomic distances used in the text and tables.

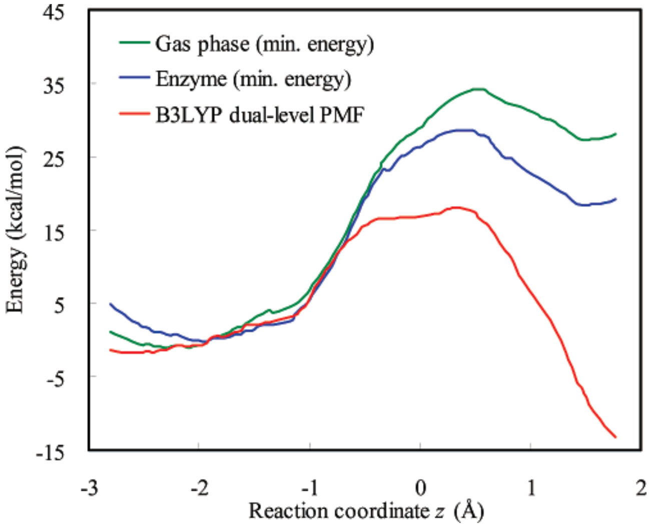

Figure 4: Computed potential of mean force and the minimum energy profiles in the gas phase and in the active site for the hydrolysis reaction of paraoxon catalyzed by phosphotriesterase.

same approach was used for smoothing out the potential at z values of +0.62 Å. This resulted in a reasonably smooth transition in these two regions.

C. The Solvated Michaelis Complex. The X-ray crystal structure of the enzyme−inhibitor complex (at pH 7.5 and 4 °C) determined at 2.1 Å resolution (PDB ID: 1DPM) is used as the starting geometry for constructing the Michaelis complex (*21*). The paraoxon-analogue, diethyl 4-methylbenzyl-phosphonate, which is an inhibitor to PTE, was used as a template for building the substrate structure (*11*, *21*). All ionic amino acid residues are set in a protonation state corresponding to pH 7. The protonation state of each histidine residue was determined by considering the possible hydrogen-bonding network with its neighboring groups in the crystal structure. Consequently, His123, His201, and His257 are neutral with the proton at the epsilon nitrogen NE2 atom. His254 is treated as protonated in the present study, although it is feasible that His254 is already deprotonated prior to the nucleophilic attack on the phosphorus center at pH 7 in view of the Brønsted plot (*18*, *25*). The rest of the histidine residues are also neutral but with the proton at the delta nitrogen ND1 atom. As a result, there are 36 positively charged residues (26 Arg, 9 Lys, and 1 His), 35 negatively charged residues (19 Asp and 16 Glu), one carbamylate group (CO_2^{2-}), one hydroxide anion, and two zinc cations in the first monomer. We added two chloride counterions to bring the total charge of the simulation system neutral. Although the second monomer of PTE does not have direct functional connections to the first active site, we have kept it during our simulation and similarly set its total charge to be neutral.

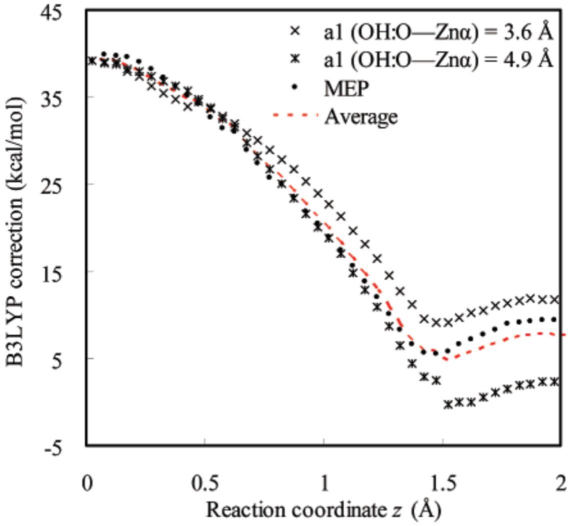

Figure 5: Computed average and individual potential energy profiles of three separate minimum energy paths for the paraoxon hydrolysis in the active site of phosphotriesterase. Energies are computed using the B3LYP//AM1:MM22 dual level potential.

For solvating the Michaelis complex, stochastic boundary conditions (*81*, *82*) were used to mimic the aqueous environment surrounding the enzyme. In this method, a water sphere of a radius of 30 Å was used to immerse the entire first monomer of PTE−substrate complex along with 262 crystal water molecules. The center of the water sphere was placed to coincide with the geometric center of the QM subsystem (Figure 1). Water molecules that are within 2.8 Å of any other non-hydrogen atoms were deleted. To avoid cavity in the system, this process was repeated three more times by randomly rotating the water sphere to another arbitrary orientation. As a result, a total of 1806 water molecules were added. Then we selected two water molecules, whose oxygen coordinates was used for the two chloride counterions. In all, the solvated Michaelis complex contains a total of 16364 atoms including 2066 water molecules.

D. Molecular Dynamics Simulations. Stochastic boundary molecular dynamics (*81*, *82*) (SBMD) simulations have been used in the present study, in which we divided the entire enzyme−solvent system into three regions, namely, the reaction region, the buffer region, and the reservoir region. Residues and water molecules that have at least one atom within 24 Å from the geometric center of the QM subsystem are included in the reaction region. The buffer region consists of residues in the layer between 24 and 30 Å from the center. All remaining atoms are assigned to the reservoir region. To imitate the effect of bulk solvent beyond the edge of the solvation sphere, a 30 Å deformable boundary potential was imposed on all water molecules (*82*, *83*). All atoms in the reservoir region are fixed throughout the MD simulations. For the reaction region, the dynamic trajectory was propagated according to Newtonian mechanics, while Langevin equations were used to describe buffer atoms with an additional harmonic restraining force to maintain the structural integrity of the system (*81*, *82*). The harmonic force constants in units of kcal mol^{-1} $Å^{-2}$ are 1.22 for backbone oxygen atoms, 1.30 for all other backbone atoms, and 0.73 for all side-chain atoms. The friction coefficients are 200 ps^{-1} and 62 ps^{-1} for all heavy atoms of protein and the oxygen atoms of water molecules respectively.

Nonbonded interactions were truncated using a force switching function between 13 and 14 Å and a potential shifting function at 14 Å for electrostatic terms and van der Waals terms respectively (*74*). The truncations were based on the center-of-mass separation between interacting groups. Bond lengths involving hydrogen atoms were constrained with the SHAKE algorithm (*84*). Dynamics of atoms were propagated using the leapfrog-Verlet integrating algorithm (*85*) with a time step of 1 fs. All MD simulations were performed using the CHARMM (version c32a1) program (*74*). Throughout the MD simulations, the atom lists for the frictions and random forces in the buffer regions were updated in every 5 time steps. The parameters and procedure of the SBMD simulations have been described (*55*, *86*−*88*).

E. Visualization. The two software packages used to visualize the calculated data and to generate the figures in this paper were Visual Molecular Dynamics (*89*) and GaussView (*90*).

2. RESULTS AND DISCUSSION

A. Free Energy Profile. Shown in Figure 4 is the dual-level potential of mean force or free energy profile (eq 7) as a function of the reaction coordinate z (eq 4), determined at the B3LYP/6-31+G(d)/MIDI!//AM1:MM22 level of theory, where the double slash indicates that the geometry used in energy corrections is determined at the AM1:MM22 level. In addition, the minimum energy profiles for the nucleophilic substitution reaction of the QM subsystems in the gas phase and in the enzyme are displayed. All three profiles have been anchored with an energy of zero at $z = -1.92$ Å, which corresponds to the value found in the X-ray crystal structure. Since the energy profiles are used only for the dual-level [$E_{QM}^{HL}(z_{LL}^{MEP}) - E_{QM}^{LL}(z_{LL}^{MEP})$] correction to obtain the PMF (eq 7), we decided not to convert these quantities into free energies in this figure. Nevertheless, it is of interest to notice that the energy barrier height of the QM subsystem is reduced from 35.1 kcal/mol in the gas phase to 28.7 kcal/mol in the enzyme along the MEP. This is accompanied by a small shift in the location of the transition state from $z = 0.53$ Å in the gas phase to $z = 0.43$ Å in the enzyme. The difference between these two energy barriers is 6.4 kcal/mol, which reflects the stabilizing effects of the enzyme on the transition state. Significantly, the potential of mean force, $W^{DL}(z)$, in Figure 4 shows a free energy barrier of 18.3 kcal/mol (eq 6), corresponding to a further reduction of 10.4 kcal/mol by including entropic contributions from dynamics simulations. The location of the transition state is further shifted to the reactant side, consistent with the Hammond postulate (*91*). The results in Figure 4 demonstrate that it is essential to carry out free energy simulations to investigate the mechanism of enzymatic reactions, whereas it is insufficient only to examine one minimum energy or free energy path in a fixed (minimized) enzyme environment.

Table 1: Computed Energy Barriers (kcal/mol)

B3LYP gas phase[a]	35.1
B3LYP enzyme[a]	28.7
B3LYP//AM1:MM22 DL-PMF[b]	18.3
MP2//AM1:MM22 DL-PMF[b]	21.4
experiment[c]	12.8

[a] Along the minimum reaction energy path (MEP) of the solvated Michaelis complex model using the dual level approximation. [b] Potential of mean force (PMF) using the dual level approximation. [c] From $k_{cat} \approx 2400$ s^{-1} and $T = 298$ K in ref (*4*).

The computed free energy barrier at the B3LYP//AM1:MM22 dual level (Figure 4) is somewhat greater than the experimental value of 12.8 kcal/mol (*4*, *15*, *24*), but the agreement is reasonable in view of the computational complexity involved in the study. If one is interested in examining the results from other high level methods, such as MP2, it can be performed simply by replacing the intrinsic energy corrections with the new high level data (Table 1). The DFT calculations yield a slightly lower barrier than the MP2 method for the PTE reaction, which is typically the case in previous studies (*17*, *92*−*94*). Table 1 summarizes the computed barrier heights by using various dual-level combinations.

Since the dual-level approximation makes use of the structures along the MEP, it is necessary to examine if the conformations explored during the umbrella sampling simulations are significantly different from the optimized structures. We find that the fluctuations of atoms in the QM region have average rmsd values of 0.7 Å for the transition state ensemble relative to the transition structure of the MEP. Greater deviations are found at large z values, corresponding to the product of the reaction. Here, the bond between the hydroxide oxygen atom and the α-zinc atom (i.e., a_1 in Figure 1B) becomes detached in free energy simulations, in contrast to the configurations optimized along the MEP, where the bond remains in the range of 2.1 to 2.6 Å. For this region, we averaged the high-level results over different reaction paths. We computed two additional MEP reaction paths on the product side by fixing OH:O−Zn_{α} at 3.6 Å and 4.9 Å, respectively. These two values were used because we found that OH:O−Zn_{α} fluctuates around these two regions during the umbrella sampling simulations and they correspond to the average results when the structures are clustered. The average results of $E_{QM}^{HL}(z)$ over these three reaction paths, starting from $z = 0$ to 2.0 Å, were used in eq 7 as the final correction terms. In Figure 5, we illustrate the three individual curves and the average HL-profile as a function of z. Interestingly, the average profile is similar to the MEP curve.

B. Transition State. A snapshot of the transition state for the phosphotriester hydrolysis is shown in Figure 2A, which

Table 2: Selected Average Interatomic Distances and Bond Angles at the Michaelis Complex State, Transition State, Transition Plateau, and Water-Recycle State in the Active Site of Phosphotriesterase[a]

label[b] (ligand:atom)	reactant state[c]	transition state[d]	transition plateau[e]	water-recycle state[f]
		Distance (Å)		
interaction with α-Zn				
a_1 (OH:O−Zn$_{\alpha}$)	2.1 ± 0.1	4.4 ± 0.1	4.2 ± 1.2	5.9 ± 0.3
a_5 (Lys169:OT2−Zn$_{\alpha}$)	2.4 ± 0.4	2.1 ± 0.1	2.4 ± 0.6	2.1 ± 0.1
a_6 (H2O:O−Zn$_{\alpha}$)	4.5 ± 0.5	4.9 ± 0.7	5.2 ± 1.0	3.3 ± 0.3
interaction with β-Zn				
b_1 (OH:O−Zn$_{\beta}$)	2.1 ± 0.1	3.8 ± 0.2	3.8 ± 0.3	4.5 ± 0.1
b_2 (P:O^{g}−Zn$_{\beta}$)	3.8 ± 0.3	2.1 ± 0.1	2.1 ± 0.1	2.1 ± 0.1
b_5 (Lys169:OT1−Zn$_{\beta}$)	2.1 ± 0.1	2.2 ± 0.1	2.2 ± 0.1	2.2 ± 0.1
b_6 (H2O:O−Zn$_{\beta}$)	6.8 ± 0.5	7.1 ± 0.5	7.2 ± 0.6	4.5 ± 0.4
zinc−zinc interaction				
c_1 (Zn$_{\alpha}$−Zn$_{\beta}$)	3.5 ± 0.1	5.3 ± 0.3	5.3 ± 0.3	5.2 ± 0.2
water-His254 interaction				
c_2 (H2O:O−His254:NE2)	6.3 ± 0.4	5.2 ± 1.0	5.1 ± 1.6	4.2 ± 0.4
bond forming/breaking				
r_{POp} (P:Op^{h}−P)	1.6 ± 0.0	1.9 ± 0.0	1.7^{i}±0.1	3.1 ± 0.1
r_{OhP} (OH:O−P)	3.6 ± 0.0	1.6 ± 0.0	1.7^{i}±0.1	1.6 ± 0.0
H-bond (donor−acceptor)				
d_1 (OH:H−Asp301:OD2)	2.4 ± 0.7	3.1 ± 0.9	3.4 ± 1.0	4.8 ± 0.4
d_2 (His254:HE2−Asp301:OD2)	2.2 ± 0.5	3.2 ± 1.3	3.0 ± 1.0	3.5 ± 0.5
d_3 (His254:HE2−P:O^{g})	5.4 ± 0.5	4.4 ± 0.6	4.5 ± 0.5	4.3 ± 0.3
d_4 (Trp131:HE1−P:O^{g})	3.7 ± 0.8	4.0 ± 0.4	4.1 ± 0.5	4.4 ± 0.3
d_5 (H2O:H−Asp301:OD2)	3.6 ± 0.6	3.4 ± 0.7	3.6 ± 1.3	2.0 ± 0.2
d_6 (OH:H−H2O:O)	4.6 ± 0.5	3.4 ± 0.6	3.7 ± 0.8	2.2 ± 0.3
		H-Bond Angle (deg)		
d_1	137 ± 20	113 ± 22	97 ± 34	125 ± 15
d_2	127 ± 18	104 ± 19	101 ± 21	92 ± 11
d_3	116 ± 14	130 ± 20	127 ± 17	127 ± 14
d_4	141 ± 14	146 ± 19	144 ± 17	116 ± 8
d_5	101 ± 30	99 ± 33	98 ± 40	161 ± 10
d_6	99 ± 9	96 ± 33	90 ± 29	139 ± 16

[a] All distances are given in angstroms, and angles in degrees. [b] See Figures 1 and 3 for the schematic diagrams representing the interatomic distances. [c] Average values over the configurations in the umbrella samplings corresponding to $z = -1.96 \pm 0.01$ Å. [d] Average values over the configurations in the umbrella samplings corresponding to $z = 0.28 \pm 0.01$ Å. [e] Average values over the configurations in the umbrella samplings corresponding to z between −0.33 and 0.33 Å. [f] Average values over the window of umbrella samplings with the harmonic force centered at $z = 1.4$ Å for the first 50 ps. [g] P:O denotes the phosphoryl oxygen atom. [h] P:Op denotes the oxygen atom attached to the nitrophenyl leaving group. [i] The average values may not be meaningful since they also depend on the number and the size of windows to sample in this plateau.

is the last configuration from the umbrella sampling simulations, corresponding to $z = 0.28 \pm 0.01$ Å. This configuration is as arbitrary as any structures in the transition state ensemble. For clarity, we also present a schematic diagram along with key geometrical parameters in Figure 3A. Figure 2A reveals that the side chain indol ring of Trp131 points toward the zinc-coordinating phosphoryl oxygen. In Table 2, we summarize the average hydrogen bond distances and angles of active site interactions in the Michaelis complex, or the reactant state ($z = -1.96 \pm 0.01$ Å), in the transition state ($z = 0.28 \pm 0.01$ Å) and the plateau region near the top of the free energy barrier ($z = -0.33$ to $+0.33$ Å), and in the product state. In the following, we highlight some key interactions that undergo significant changes from the Michaelis complex to the transition state.

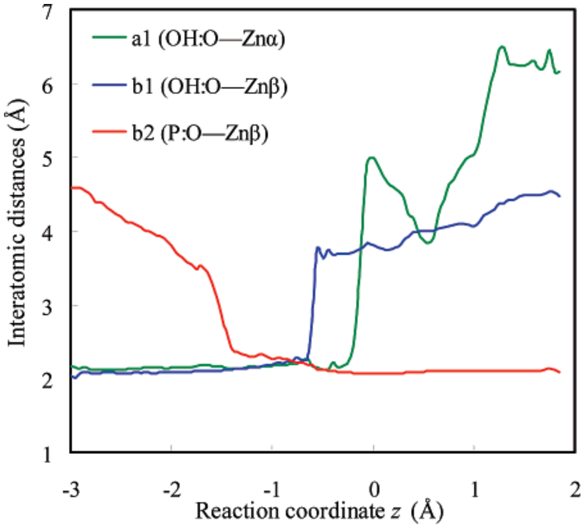

FIGURE 6: Variations of interatomic distances of the nucleophile hydroxide ion from both zinc atoms, and the distance between the divalent phosphoryl oxygen and the β-zinc ion, as a function of the hydrolysis reaction coordinate.

Bimetallo-Zinc Center. In the Michaelis complex, the active site of PTE contains two zinc ions that are located at an average distance of 3.5 ± 0.1 Å and are bridged by the carbamylate group of Lys169 and a hydroxide ion (Figure 1). The key issue underlying the catalytic mechanism of PTE is the structural motions of the binuclear center and the associated ligands accompanying the chemical process. Table 2 lists the average values of some key geometrical variables in the reactant (Michaelis complex) state, and in the transition state, while Figures 6−8 depict the variation of some of these average distances as a function of the reaction coordinate. The present study shows that the nucleophile hydroxide ion loses its coordination to the binuclear center as a result of the substitution reaction at the phosphorus center. Comparing with the PMF in Figure 4 and the interatomic distances shown in Figure 6, we notice that the coordination of the nucleophile hydroxide oxygen to Zn$_{\beta}^{2+}$ (OH:O−Zn$_{\beta}$) breaks

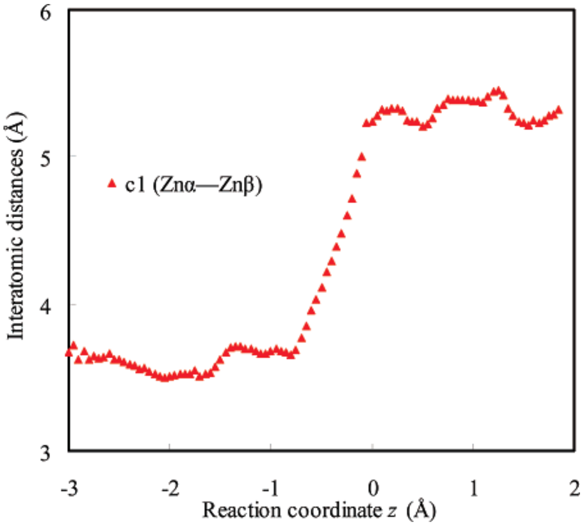

FIGURE 7: Variation of the bimetallo center zinc−zinc distance as a function of the hydrolysis reaction coordinate.

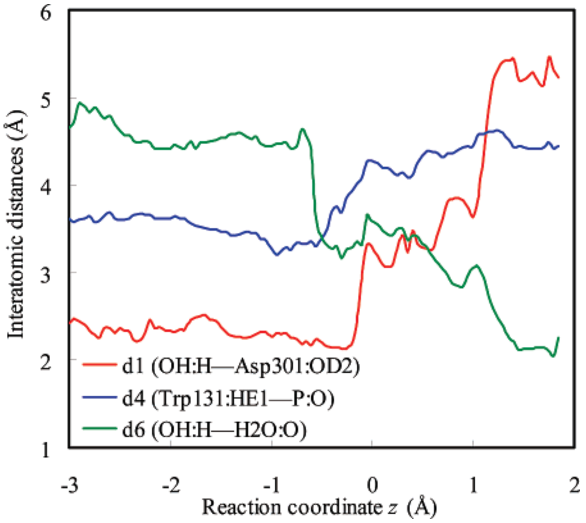

FIGURE 8: Variations of the hydrogen-bond distances between the hydroxide ion and Asp301, between Trp131 and phosphoryl oxygen, and between the hydroxide ion and a water molecule, as a function of the hydrolysis reaction coordinate.

rather early along the reaction path, at $z = -0.6$ Å, as soon as the free energy shows steep increase. The average distance of the bridging oxygen increases from 2.1 ± 0.1 Å in the Michaelis complex to 3.8 ± 0.2 Å in the transition state. As a result, electrostatic coordinating forces are weakened between the hydroxide ion and Zn_{β}^{2+}. Concomitantly, the $Zn_{\alpha}-Zn_{\beta}$ distance increases to 5.3 ± 0.3 Å at the transition state (Figures 2 and 7).

Figure 9 compares the structures between the Michaelis complex and a snapshot of the transition state complex by superpositioning backbone coordinates within 25 Å of the reaction center. The relatively large change in zinc separation is easily accommodated by collective shifts of the side chain conformations, while the backbone structures show relatively smaller changes. The present results show that the average motions of the two zinc ions are directly correlated to the reaction coordinate motion, a similar feature also found in xylose isomerase both from X-ray structural determination (*96*, *97*) and from QM/MM simulation studies (*87*, *88*).

The phosphoryl oxygen shortens its distance from Zn_{β}^{2+} ion to a value of 2.1 Å (P:O−Zn_{β} in Figure 6). Interestingly, this transition occurs rather early as well along the reaction coordinate. The thermofluctuations and structural changes of the phosphoryl group, leading to early tight-binding to the metal, is important for activation of the phosphorus center, and this is in good accord with experimental findings by Raushel and co-workers, who observed enhanced effects on thiophosphotriester substrate, which requires greater P═S bond activation (*18*, *95*). A further benefit is that as the phosphoryl oxygen binds more strongly to the β-zinc ion, it facilitates the dissociation of the bridging hydroxide ion (Figure 6), hence increasing its nucleophilicity.

While this article was being prepared, Chen et al. reported DFT calculations for a model PTE active site, consisting of the substrate and inner sphere ligands (*98*). The B3LYP functionals along with 6-31G(d,p) and LANL2DZ basis sets were used for organic species and zinc ions, respectively. The results provide further assessment of the potential function used in the present simulations. Chen et al. followed the reaction path proposed by Raushel and co-workers, obtaining a final product complex that has a phosphodiester bridged to both zinc ions along with a protonated Asp301 from the hydroxide nucleophile. The $Zn_{\alpha}-Zn_{\beta}$ separation changes from 3.54 Å in the reactant to 4.34 Å in the product complex. Inspecting the structures from ref (*98*), we noticed that the nitro group (an oxygen atom) of *p*-nitrophenolate ion is only 1.65 Å from one of the immidazole hydrogen atoms (*98*), whereas in the dynamics simulations, the leaving group is located in a different region of the active site at least 7 Å away, and is exposed to the solvent. This illustrates the potential problems often encountered by geometry optimization of active site models in the gas phase. We have further examined the product complex structure, excluding the *p*-nitrophenolate leaving group, by B3LYP/6-31G(d) optimizations, and located two minimum structures, corresponding to the proton located on Asp301, and on the nucleophile hydroxyl group. The optimized $Zn_{\alpha}-Zn_{\beta}$ distances are 4.42 and 4.78 Å, respectively (Supporting Information). The latter corresponds to the protonation state of the product complex found in the present QM/MM simulations. When this complex (unprotonated Asp301) was optimized by the AM1 model, we obtained a $Zn_{\alpha}-Zn_{\beta}$ separation of 4.86 Å. Moreover, the bond between Zn_{α} and OH:O in this complex is broken for both B3LYP (3.33 Å) and AM1 (3.42 Å) structures. Overall, the AM1 structure is similar to the B3LYP structure for this product complex (Supporting Information). These results, together with the AM1:MM22 Michaelis complex discussed earlier, suggest that the AM1 geometries from the simulation study are adequate from the reactant to product states, in comparison with the experimental and DFT data.

His254. In the Michaelis complex, His254 is hydrogen bonded to the anti lone pair of OD2 of Asp301, whose other carboxyl oxygen is coordinated to Zn_{α}^{2+}, at an average distance of 2.1 Å (Table 2). As the reaction coordinate reaches the transition state, the side chain of His254 moves away from Asp301 toward the oxyanion of the leaving group, decreasing the distance His254:HE2−P:O by more than 1 Å to a value of 4.4 ± 0.6 Å in the transition state. Concomitantly, His254:HE2−Asp301:OD2 is lengthened to 3.2 ± 1.3 Å, accompanied by a rotation of the imidazole ring by about 15°. Notice that His254 is rather mobile with large thermofluctuations along the entire reaction coordinate,

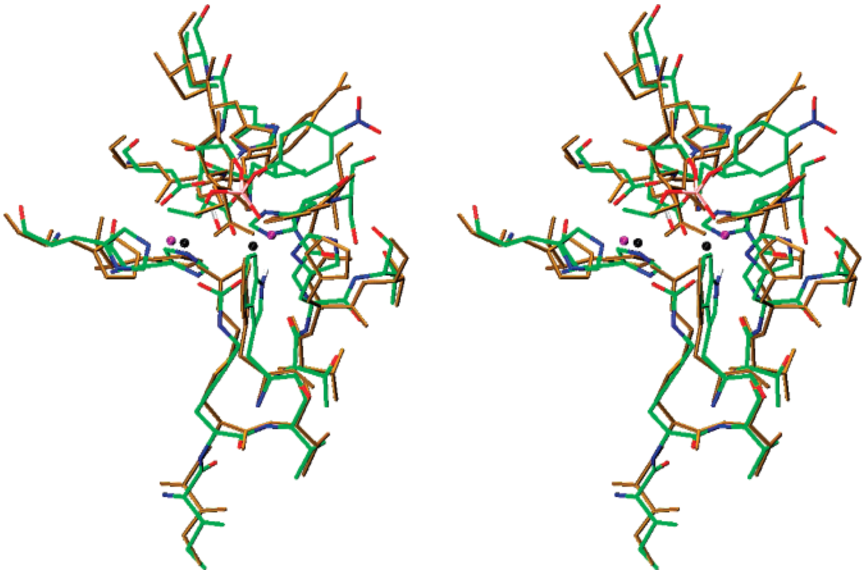

FIGURE 9: Comparison of the structures between snapshots of the Michaelis complex and the transition state by superpositioning the backbone atoms within 25 Å from the active center. The Michaelis complex is shown in color for the active site residues, and the zinc ions are in black. The transition state structure is shown in gold with zinc atoms highlighted in pink. Residue identities can be located by comparison with the structure in Figures 2 and 3.

suggesting that His254 does not play a precisely defined role in catalysis. Throughout the simulations, His254 retains ion pair interactions with Asp233 on the opposite side. QM/MM electrostatic energy decomposition analyses (*99*) indicate that His254 interacts more favorably with the transition state by −9 kcal/mol than the interaction energy in the Michaelis complex; however, the rmsd is large (±29 kcal/mol). Thus the change in interaction energy does not have quantitative significance.

Trp131. The role of Trp131 is less obvious simply by considering its energy contributions because there is little variation in the computed QM/MM electrostatic energy along the reaction path (0 ± 30 kcal/mol). The average hydrogen bond distance between Trp131 and the phosphoryl oxygen O1 (Trp131:HE1−P:O) only has small variations between the reactant state (3.7 ± 0.8 Å) and the transition state (4.0 ± 0.4 Å). However, it is interesting to point out the trends of its change along the reaction pathway (Figure 8), and the average distance reaches the minimum at $z = -1$ Å at the footstep of the free energy bottleneck. As a result, we propose that the role of residue Trp131 is not for TS stabilization, but it is mainly for substrate binding and positioning its orientation in the active site.

Transition Plateau. Unlike typical S_N2 reactions in solution, which shows a sharp and unimodal free energy profile (*70*, *100*), the present phosphotriesterase-catalyzed reaction has a rather flat free energy profile near the highest point along the PMF. Interestingly, similar features have been observed in the dianionic methanolysis of cyclic phosphates in solution (*101*). In a recent study of the active site cluster complex using B3LYP/6-311+G(2d,2p) calculations, Chen et al. reported a very similar reaction profile that shows a remarkably similar, broad plateau region for the transition state (*98*). We call this region the transition plateau, which spans the range from $z = -0.33$ to 0.33 Å (Figure 4). We have averaged the key structural parameters for all structures sampled during the free energy simulations over this entire range, which are also given in Table 2. Interestingly, the average values over the transition plateau are very close to those obtained for structures in the "bin" with the highest energy, the transition state. The greatest variation is associated with the hydrogen atom of the nucleophilic hydroxide ion. In particular, the distance between the hydrogen atom of the bridging hydroxide ion and the OD2 oxygen of Asp301 (OH:H−Asp301:OD2) is about 0.3 Å longer in the average over the plateau structures than that at the transition state, and the hydrogen bonding angle is bent by 16° from linearity as it is found in the transition state (Table 2). This suggests that the analyses of structural and energy contributions to the transition state stabilization from His254 and Trp131 using structures at the top of the reaction barrier are reasonably representative.

C. The Water-Recycle Resting State. The PMF from umbrella sampling simulations were not extended further beyond the reaction coordinate $z = 1.8$ Å (Figure 4) because the overall active site dynamics can no longer be adequately described by z. The chemical step has been considered to be irreversible because of the large free energy of hydrolysis (*25*). In particular, as the nucleophile hydroxide ion forms a chemical bond with the phosphorus center, a greater cavity is generated in the active site, and a water molecule from the bulk solvent gradually enters the binding site between the two zinc ions (Figures 2B and 3B). This "dynamical" exchange of water molecules in the active site occurs in the last two simulation windows centered at $z = 1.4$ and 1.7 Å. At first, one water molecule resides in the zinc ion bridging position for more than 50 ps in the 1.4 Å window before it diffuses away and is substituted by another water molecule. In the next window (at $z = 1.7$ Å), the initial water molecule diffuses back into the ligand position and stays for the entire simulation. Figure 10 shows the histogram of the oxygen−zinc distances for the two water molecules over the 100 ps trajectory during the umbrella sampling simulations, which reflects the dynamic feature of the solvent−ligand binding/coordinating interactions in the active site. Specifically, the average distances between the first water molecule and the α-zinc ion (H2O:O−Zn_α or a_6 in Figure 3B) or β-zinc ion (H2O:O−Zn_β or b_6 in Figure 3B) are 3.3 ± 0.3 and 4.5 ±

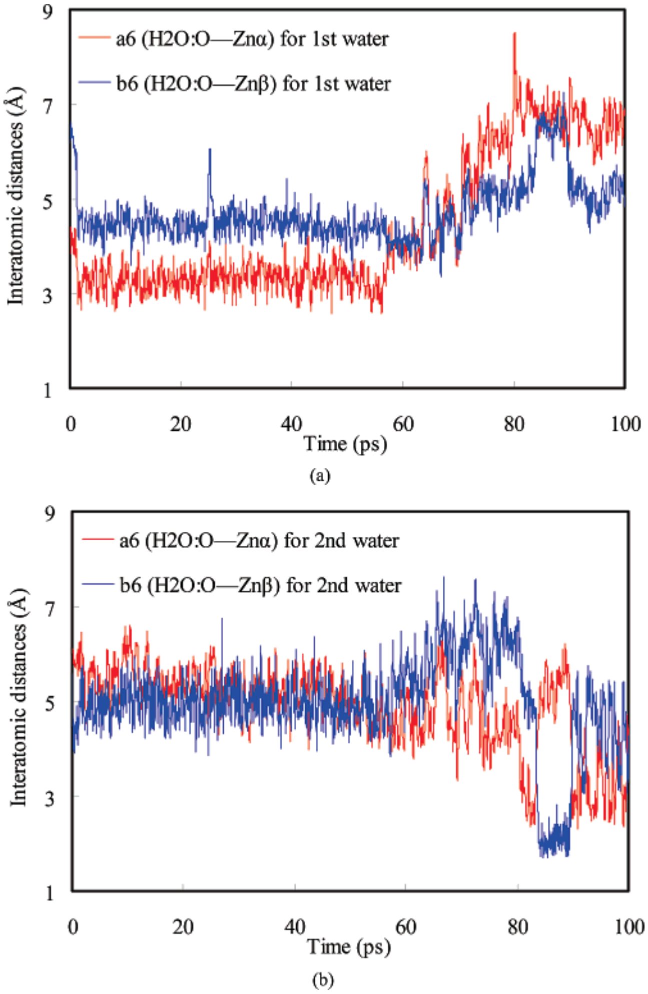

FIGURE 10: Histogram of the distances between a water molecule and the two zinc ions in the active site of phosphotriesterase during the umbrella sampling simulations. (a) One water molecule is seen to migrate away from the active site after 50 ps in the window at $z = 1.4$ Å. (b) As the first water leaves the active site, the second water enters the binding site to the two zinc ions.

0.4 Å, respectively, over the first 50 ps (Table 2 and Figure 10a), and these were replaced by the second water in the last 20 ps as they exchange positions (Figure 10b).

Several key hydrogen bonding interactions are found to help stabilizing the water molecule in the active site, and analyses of these hydrogen bonding interactions prompt us to propose that the nucleophilic hydroxide ion is generated by a proton transfer from this water to His254 either directly or via a proton relay through another water molecule. Alternatively, the proton transfer may take place directly into the bulk solvent as the pK_a of water bounded to zinc ions is sufficiently low, e.g., about 7 in carbonic anhydrase (*102*). Figure 8 illustrates that the entrance of this water molecule into the active site is highly correlated with the reaction coordinate by hydrogen bonding interactions with the hydroxyl hydrogen of the nucleophile (OH:H$-$H$_2$O:O or d_6 in Figure 3B). In addition, one of the hydrogen atoms of the water molecule is hydrogen bonded to Asp301 at an average distance of 2.0 ± 0.2 Å, which is present in the Michaelis complex. These findings allow us to propose a revised mechanism for the phosphotriesterase catalytic cycle, which also points to the directions for further studies of PTE.

3. AN ASSESSMENT OF ENZYME MECHANISM BASED ON CRYSTAL STRUCTURE AND COMPUTATION

A key result of this study is a revision of the proposed mechanism of the PTE catalyzed phosphate hydrolysis reaction (*18*). Based on kinetic data, mutations, and crystal structures of homologous enzymes and enzymes belonging to the same superfamily, Raushel proposed a sequence of events that feature a key binuclear-bridged intermediate between the product and the zinc ions (*18*). Although the mechanism of ref (*18*) is very reasonable, it is not clear how this potentially very stable intermediate is further hydrolyzed and removed from the active site. This poses a kinetic difficulty for this nearly diffusion controlled reaction. The revised mechanism does not involve this binuclear-bridged intermediate as a result of the combined QM/MM dynamics simulation, and provides a process for the release of the phosphodiester product (see below). This involves the delicate balance in coordination number and net charge of the ligands that coordinate the metal ions. In this section, we address the issue of interpretation of X-ray crystal structures in assessing enzyme mechanisms.

In the Michaelis complex, each zinc ion enjoys a total of five ligands (two are shared through the ligand bridges) with a distorted trigonal bipyramidal geometry. The question of coordination number to zinc ions has been extensively investigated, through molecular dynamics simulations and molecular orbital DFT calculations of active site models (*12*). The present results, which utilize a combined QM/MM potential in molecular dynamics simulations, are in excellent agreement with the conclusions from the thorough investigations by Zhan et al. (*12*), and with all existing X-ray structures (*4*, *21*, *22*), supporting that the AM1:MM22 potential is a reasonable model for the PTE system (Supporting Information).

As the nucleophilic reaction reaches the transition state, the separation between Zn_α^{2+} and OH:O also becomes greater (OH:O$-$Zn$_\alpha$ in Figure 6). At this stage, a water molecule enters the metal binding pocket, replacing the hydroxyl ligand. The zinc ion retains its pentacoordination number. Interestingly, its distance to the carbamylate OT2 (Lys169: OT2$-$Zn$_\alpha$) oxygen is reduced by 0.3 Å, gaining stronger interactions with one of its ligands (Table 2).

The PTE phosphotriester hydrolysis reaction has a rather late transition state where the chemical bond between the phosphorus and the oxygen atom of the hydroxide ion is formed ($r_{OhP} = 1.61$ Å), and the bond of the leaving group is largely cleaved ($r_{POp} = 1.88$ Å). This reaction profile is in good accord with ^{18}O isotope effects (*29*) and Brønsted analyses (*18*, *25*), supporting a late transition state in the PTE hydrolysis reaction of paraoxon substrate. Another noticeable change is the hydrogen bond between the hydroxyl hydrogen of the nucleophile and Asp301 (OH:O$-$Asp301: OD2), which is elongated by 0.7 Å to a value of 3.1 Å as the hydroxyl group moves away toward the phosphate substrate in the transition state (Table 2 and Figure 8). It is important to emphasize that both at the transition state and in the hydrolyzed product$-$enzyme complex, the oxygen atom originating from the nucleophile hydroxide ion is no longer coordinated to the bimetallo-centers (Figures 2B and 3B), and only one oxygen from the phosphate diester product is coordinated to Zn_β^{2+} ion. This configuration is a key new aspect of the revised mechanism, different from that proposed previously (*4*, *18*, *21*).

An anonymous referee pointed out that a binuclear-bridged crystal structure has been determined for dimethyl thiophosphate (DMTP) with the PTE from *Agrobacterium* (*103*), a homologous enzyme with 90% sequence identity, and that similar structures have been determined in several other enzymes containing two metal centers, including urease (PDB ID: 3UBP) (*104*), iso-aspartyl dipeptidase (PDB ID: 1ONX) (*105*), and dihydroorotase (PDB ID: 1J79) (*95*). Although different metals are involved, a common feature in these crystal structures is that the distances between the two metal ions in the active site do not undergo significant change in comparison with the apoenzymes, and these structures have been proposed as evidence representing the reaction intermediates of these enzymatic reactions. The difficulty of correlating analogous crystal structures with enzyme mechanism is a struggle that we constantly face, computationally and otherwise; how and to what extent can we use the stable structures of enzyme complexes, observed under crystallization conditions, as models to interpret the mechanism and transient species generated during a chemical transformation? The main difficulty is that these structures are too stable to be useful for catalyzed reactions, often at rates approaching the diffusion limit, whereas the native substrates are typically transformed into the products before the Michaelis complex structures can be determined (except a few rare cases). On the other hand, these model structures determined by X-ray crystallography provide the best structural information relevant to the reaction mechanism. However, their interpretation is best achieved with the aid of computation by modeling the free energy profile along the reaction path. To address this question, we carried out further simulations of the binuclear-bridged complexes.

First, we mention a related work on the dynamic motions of metal ions in the active site. Although the structures noted above show little metal variations in these enzymes, careful experiment and design of transition-state analogues can yield remarkably informative insight as illustrated in the study of xylose isomerase (*96*, *97*), an enzyme containing two metal ions bridged by a carboxylate similar to that in PTE. Lavie et al. reported two positions for the second, mobile Mg^{2+} ion in the D-xylose complex with distances of 3.8 and 5.4 Å from the first metal ion (*96*). The authors attributed this observation to a mixture of the substrate and product complex in the crystal and the longer metal separation corresponds to the product structure. Subsequently, Allen at al. designed a transition state analogue, whose structure shows an elongated metal separation of 4.2 Å (*97*), intermediate of the Michaelis and product complexes. Employing the same computational technique, we obtained exactly the same trend of metal ion migrations, which we called a breathing mechanism in xylose isomerase (*87*, *89*). Interestingly, in another crystallographic study (*106*), the coordination pattern of the mobile Mg^{2+} ion was found to be different from that in ref (*96*). Our computational results (*87*, *89*) were only consistent when the latter coordination arrangements (*106*) were used, but the mechanistic interpretation is a combination of both sets of crystal structures and computational results (*96*, *106*).

We performed additional simulations to examine the possibility of forming a stable bridged complex if we prepare our simulations with a phosphodiester anion as the substrate. We constructed this configuration by removing the proton from the nucleophile and neutralizing the leaving group *p*-nitrophenol, making use of the product structure from the free energy simulations. After equilibration, this binuclear-bridged conformation remains stable after 100 ps with an average Zn−Zn distance of 4.7 ± 0.2 Å (additional data are given in Supporting Information). To compare with the crystal structure of DMTP with the *A.*-PTE (PDB ID: 2D2G) (*103*), we also performed a simulation using the DMTP substrate in the present *Pseudomonas diminuta* PTE. Despite the major difference in coordinations (octahedral to two Co^{2+} ions in the *A.*-PTE (*103*) structure versus twisted bipyrimid to Zn^{2+}) (*21*), a stable structure was also obtained after 100 ps dynamics simulations (Supporting Information). These simulations show that the potential energy functions used in this study can indeed yield a reasonable description of the binding properties of the binuclear active site, consistent with the X-ray structure (*103*).

This raises an important and general question concerning the use of crystal structures to interpret the enzyme mechanism. Undoubtedly, the structural information provides key insight into the binding and function of the enzyme activity. However, as noted before, these complex structures must be stable enough for X-ray diffraction experiments, and it is highly likely that they do not correspond to the exact intermediate species in the enzymatic process. For the PTE enzyme, the authors of ref (*103*) lucidly pointed out that "the formation of a dually bound product, which is stable enough, and its departure slow enough, to be observed in a complex with the enzyme is *inconsistent* (italic by us) with the diffusion limited hydrolysis of parathion." They further predicted that "if no dually bound product forms during parathion hydrolysis, ... this weak coordination would permit the rapid departure of the products and the extremely high catalytic rates observed during catalysis" (*103*). The present study has not addressed the question of the free energy barrier for removing a bridged diethyl phosphate anion ligand. Other experiments show that the hydrolysis rate is determined by the pKa value of the leaving group for a series of substituted phenyl groups (*25*).

Our combined QM/MM simulation shows that the binuclear-bridged intermediate is not formed as a result of the nucleophilic attack by the hydroxide ion if the hydroxyl proton is not lost to the solvent as the product is immediately formed (Figures 2 and 3). Yet, a stable binuclear-bridged complex can be produced when the product anionic substrate is coordinated to the zinc centers as the starting structure. The difference appears to be due to the protonation state of the phosphodiester. It has been proposed that a proton transfer occurs from the nucleophile hydroxyl group to Asp301 (*18*), but this would neutralize the ligand to a metal ion with +2 au charge. The acidity of this Zn^{2+}-coordinated Asp residue would be too high to accept a proton from a phosphodiester if a bridged enzyme-product complex is not formed. Importantly, a water molecule diffuses into the active site to coordinate with the metal ion and to donate a hydrogen bond to Asp301 (Figures 2B, 6, and 10). Experimentally, although the bridged DMTP complex structure can be obtained by soaking the enzyme crystal with the slow substrate dimethoate, Scheme 2: Proposed Mechanism for the Hydrolysis of Paraoxon by Phosphotriesterase

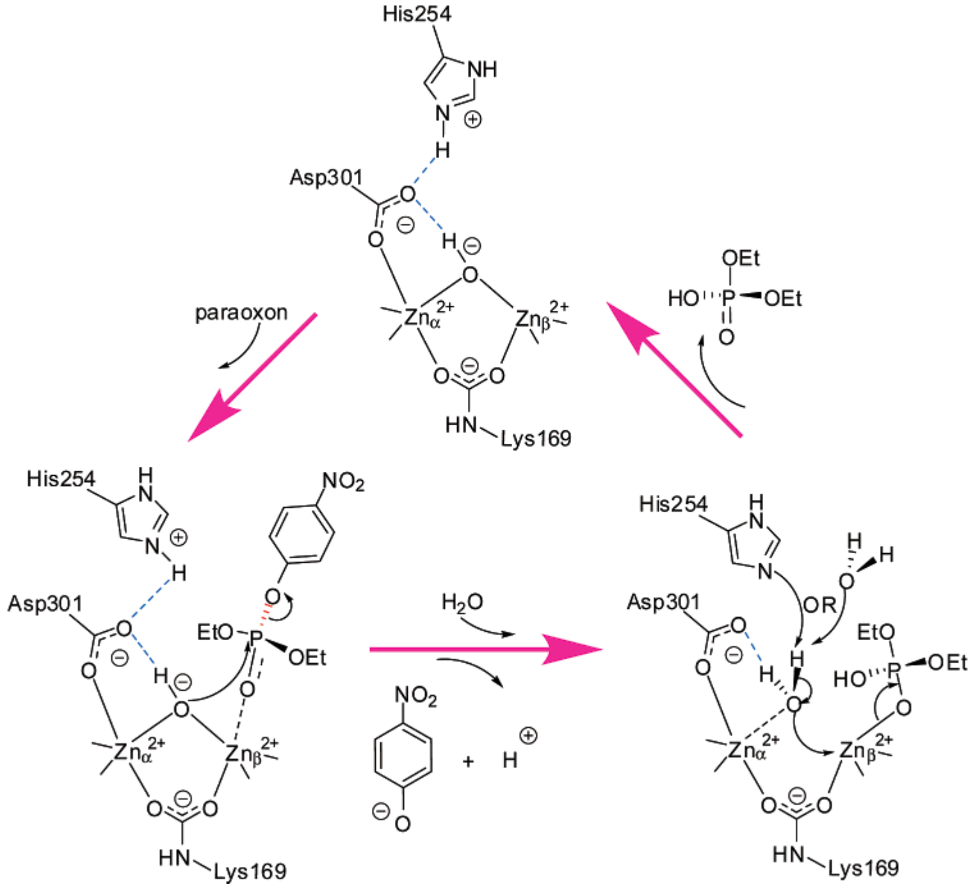

it was not possible to obtain any trace of DMTP in the crystal if the substrate parathion is soaked and hydrolyzed to yield DMTP (*103*). The difference in the X-ray structures between these two substrates suggests that the product of the slowly hydrolyzing substrate has sufficient time to lose a proton and to form a stable bimetallo-bridged complex. In previous studies, we have discussed this difference between the enzyme−substrate complex produced during the enzymatic process and that obtained by equilibrium binding of the product under crystallization conditions (*19*, *107*, *108*). Here, we document computational results, suggesting that the difference in PTE enzyme can be attributed to the protonation state of the phosphodiester product: the proton remains on the nucleophile immediately after the reaction, and it is deprotonated from equilibrium solvation in solution.

4. PROPOSED MECHANISM

Based on the mechanism proposed by Raushel and co-workers (*18*), and through the analyses of the potential of mean force, the changes in hydrogen bonding interactions of active site residues, and the dynamical interactions of water molecules in the bimetallo-zinc binding site, we propose a detailed mechanism for the catalytic cycle of phosphotriesterase (Scheme 2). In this model, the substrate paraoxon first binds to the active site by loosely coordinating its divalent phosphoryl oxygen to the β-zinc ion, which is more solvent exposed in the apoenzyme. At this stage, the two zinc ions in the active site are bridged by the carbamylate group (Lys169) and the nucleophile hydroxide ion, and each zinc has five coordinates in a distorted trigonal bipyramidal geometry. The structural features of the Michaelis complex are identical to that proposed in ref (*18*).

The chemical step occurs through nucleophilic attack on the phosphorus center by the bridging hydroxide anion. Experimentally, Raushel and co-workers concluded that, for good leaving groups such as *p*-nitrophenol with a pK_a of 7.1, the chemical step is not entirely rate-limiting, but the step to regenerate the resting state accompanied by a proton abstraction of the nucleophilic water is the rate-limiting process (*18*). In the nucleophilic substitution reaction, a number of interactions undergo significant changes along the reaction pathway. First, the phosphoryl oxygen forms a stronger coordination by shortening its distance to the β-zinc ion (Figure 6), which provides polarization activation of the P═O bond, a proposal originally suggested by Raushel and co-workers, and it is confirmed by their elegant experiments (*18*, *25*). Second, the enhanced phosphoryl coordination to the zinc ion weakens its interactions with the bridging hydroxide ion, but increases the nucleophilicity of OH^-, a proposal also made in ref (*18*). The S_N2 attack by the hydroxide ion is accompanied by loss of its bridging coordinations to both zinc ions (Figure 6). Third, a water molecule, originally having hydrogen bonding interactions with Asp301, occupies the space of the hydroxide ion by forming a coordinating interaction with the α-zinc ion (Figures 2B and 3B), and this water molecule can exchange with other bulk water molecules dynamically. Although the coordination numbers are retained by both zinc ions, a consequence of losing the bridging hydroxide coordination, effectively transferring a net of −1 au charge to the leaving

Scheme 3

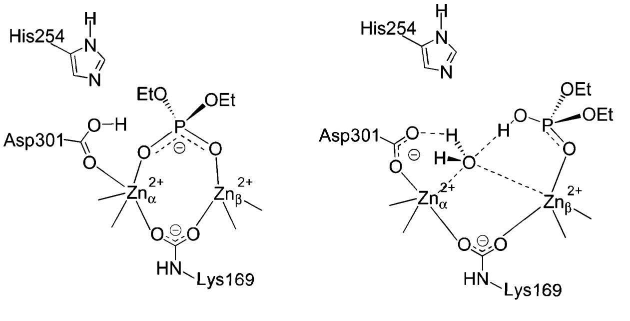

Raushel Product Intermediate Present Product Complex

group away from the two dinuclear metal center, is elongation of the inter-zinc distance from 3.5 to 5.3 Å due to electrostatic repulsion (Table 2 and Figure 7).

The third major step in the PTE catalytic cycle is to regenerate the active nucleophile, hydroxide ion, in the resting state, and this is accomplished by a proton transfer from the water molecule in the active site to His254 either directly or through an intervening water relay. Since this binuclear-bridged water is highly acidic, it is likely that the proton is directly lost to the solvent without the assistance of His254. As the proton transfer takes place, the hydroxide ion forms bridging coordinating interactions with both zinc ions, which results in (1) the shortening of the zinc−zinc distance to the compact form at an average value of about 3.5 Å and (2) the displacement of the phosphoryl oxygen ligand at the β-zinc center. The latter process is further facilitated by an anionic ligand replacing a neutral ligand, which allows the hydrolyzed phosphoryl diester to depart from the active site. This restores the active form of the apoenzyme for the next turnover.

Although the overall process is similar to the mechanism proposed by Raushel and co-workers (*18*), the present mechanism also differs from the previous model in several aspects (*18*). In the early model, the hydroxide ion loses its proton to Asp301 as it attacks the phosphoryl center. It was proposed that the resulting phosphatediester anion forms a bridge (Scheme 3), using two phosphate oxygen atoms to coordinate both zinc ions as the product−enzyme complex. This poses a difficult situation for product release in that a negatively charged phosphate ion must be separated from two divalent cation centers with the overall charge of the inner ligand sphere being always positive (+1 au in the Michaelis complex, and +2 au in the product complex). In our model, we propose that only the P═O oxygen is ligated to one zinc ion, Zn_β^{2+}. We suggest that the phosphodiester product is neutral in the enzyme active site (supported by both DFT and QM/MM calculations), but it is possible to lose a proton to the bulk solvent prior to, during, or after diethyl phosphate departs from the active site. In our model, the proton transfer from the nucleophilic water is coupled with the product release step, which is further assisted by the formation of the hydroxide ion, bridging the two zinc ions. This coordination process helps to displace the phosphate ligand to the β-zinc ion (Scheme 2). This process competes with the chemical step as the overall rate-limiting step.

In our mechanism, His254 is protonated at or below pH 7 throughout the chemical step, and it loses its proton to the solvent as the leaving group departs from the active site. In the following step, His254 acts as a base to activate and deprotonate the water nucleophile; however, we emphasize that its role as a specific or general base is *not essential* in our mechanism because the pK_a of a zinc-bound water is sufficiently low to be ionized by the solvent (a pK_a of about 6 was found for the PTE enzyme) (*18*, *101*). In the early model, His254 is neutral in the Michaelis complex and serves a role to relay the proton from the hydroxide ion through Asp301 (*18*). Although in principle the proton relay mechanism is possible, it must involve (a) the neutralization of Asp301, which is a poor base due to its coordination to a divalent metal cation, and (b) an additional step of torsional rotation of the hydroxyl group from the syn-conformation to the anti-conformation to orient the proton toward His254. Asp301 is an important residue for the PTE enzyme because it plays the role of charge balance in the binuclear metal active site. Mutations of Asp301 to Ala and Asn reduce the rate constant by 200 and 5000, respectively. The activity of the mutants may be due to rescue by a hydroxide ion as the ligand to the zinc ion (*18*). In the present mechanism, the role of Asp301 is primarily coordinating the more buried metal ion.

The variations in k_{cat} upon His254 mutations are particularly intriguing. When His254 was replaced by an alanine or an asparagine, the rate constant was *reduced* by 1−2 orders of magnitude for hydrolysis of the *fast substrate* paraoxon (*18*). This is consistent with the present mechanism because the rate-limiting step for paraoxon is after the hydrolysis, and is associated with the proton abstraction and regeneration of the resting state (*18*). If His254 actively acts as a base, it shall directly affect the rate-limiting step of the fast substrates, reducing the observed rate constant. On the other hand, the rate constant is slightly *increased* by a factor of 1.3 and 33 with the Ala and Asn mutation relative to the wild-type enzyme, respectively, when a *slower substrate* (by a factor of 64,000 compared to paraoxon), diethyl *p*-chlorophenyl phosphate, is used (*18*). In this case, the rate-limiting step is the chemical transformation, and the mutation of His254 on the proton abstraction rate has an insignificant contribution to the observed k_{cat} (a factor of 100 in the paraoxon substrate, which is much smaller than the change to a slower substrate). Currently, it is not clear about the origin of the small increase in the kinetic parameter, which may be due to long-range electrostatic effects. We are in the process of addressing the resting-state regeneration step, which may help to explain these findings.

Finally, the proposed mechanism is also consistent with the observed solvent isotope effects, which is greater for paraoxon (2.0) than diethyl *p*-chlorophenyl phosphate (1.3) since proton transfer from the nucleophilic water is more rate-limiting in the former than the latter. It is also consistent with the slight increase in solvent isotope effects for paraoxon by the mutants (2.5 for H254A) because of increased barrier height of the rate-limiting step to result in greater isotope effects.

5. CONCLUSIONS

Molecular dynamics simulations employing combined QM/MM potentials have been carried out to investigate the reaction mechanism of the hydrolysis of the phosphotriester substrate paraoxon by phosphotriesterase (PTE). The enzyme PTE has the ability to hydrolyze a wide range of organophosphate triester compounds including pesticides and insecticides as well as chemical warfare agents, and it has a great potential for use in bioremediation of environmental contaminants. To determine the potential of mean force for the paraoxon hydrolysis, we used a dual-level QM/MM approach that synthesizes accurate results from high-level electronic structure calculations with computational efficiency needed for enzyme configurational samplings. In particular, the intrinsic (gas-phase) energies of the active site in the QM region are determined by using density functional theory (B3LYP) and second-order Møller-Plesset perturbation theory (MP2) and the molecular dynamics free energy simulations are performed by using semiempirical QM/MM interactions. This resulted in a computed PMF for the paraoxon hydrolysis by PTE at an accuracy of the B3LYP or MP2 level of theory.

A key feature of the active site of PTE is a binuclear zinc-center, in which each zinc ion is coordinated to five ligands in a distorted trigonal bipyramidal structure. A carbamylate group from Lys169 and the nucleophile hydroxide ion both form bridged coordinations to the two zinc ions in a compact conformation with an average zinc−zinc distance of 3.5 ± 0.1 Å. The P═O bond of the substrate paraoxon is activated by adopting a tight coordination to the β-zinc ion, and releases the coordinate to the hydroxide ion, increasing its nucleophilicity. This resulted in a loose binuclear conformation, characterized by an average zinc−zinc distance of 5.3 ± 0.3 Å at the transition state, a feature also found in xylose isomerase by X-ray structures and computations (*87*, *88*, *96*, *97*). We propose that His254 is protonated in the Michaelis complex at or below pH 7, forming hydrogen bonds to Asp301 (a ligand of the Zn_α^{2+} atom). As the chemical step takes place, His254 is reoriented toward the oxyanion of the leaving group, and we suggest that its proton is released to the solvent as the leaving group departs the active site. It was also found that a water molecule subsequently enters into the binding pocket of the loosely bound bimetallo-center, originally occupied by the nucleophilic hydroxide ion. Although further computational studies, specifically on the product release step, are ongoing, we suggest that the proton of this water molecule is taken up by His254, and, concomitantly, the resulting hydroxide ion pulls the β-zinc ion closer to form the compact configuration and displaces the phosphodiester product ligand, which retains the overall coordination to both zinc ions to be five. This restores the resting state of the PTE enzyme for the next turnover. We note that the role of His254 as a base is not essential in view of the relatively low pK_a of a zinc-bound of water molecule.

The present mechanism suggests that the structural motions of the two zinc ions are closely correlated to the motion of the reaction coordinate. This feature has been observed in a previous study of the hydride transfer reaction catalyzed by xylose isomerase, which consists of a bimetallo-magnesium center, involving a similar breathing dynamic motion in the catalytic cycle (*87*, *88*, *96*, *97*). It would be interesting to design experiments to investigate such structural motions involving metal ions during catalysis to test the present computational results. To further quantify our proposed mechanism, we are currently investigating the free energy profile for the product-release step.

ACKNOWLEDGMENT

We thank Dr. Shuhua Ma and Dr. Yao Fan for computational assistance and advice.

APPENDIX. POTENTIAL OF MEAN FORCE USING DUAL-LEVEL POTENTIAL FUNCTIONS

The PMF corresponding to the dual-level (DL) potential energy surface (eq 3) can be obtained by free energy perturbation theory (*78*):

$$W^{\mathrm{DL}}(z) = W^{\mathrm{LL}}(z) + \Delta W^{\mathrm{HL}}_{\mathrm{QM}}(z) \qquad \mathrm{(A1)}$$

where

$$\Delta W^{\mathrm{HL}}_{\mathrm{QM}}(z) = -RT\,\ln\langle \mathrm{e}^{-[E^{\mathrm{HL}}_{\mathrm{QM}}(z)-E^{\mathrm{LL}}_{\mathrm{QM}}(z)]/RT}\rangle_{\mathrm{LL}} + \Delta W^{0} \qquad \mathrm{(A2)}$$

In eqs A1 and A2, $W^{\mathrm{DL}}(z)$ is the dual-level PMF, $W^{\mathrm{LL}}(z)$ is the lower-level PMF, which is determined directly by using the semiempirical AM1:MM22 potential in the present study, ΔW^0 is the energy difference between high and lower levels of theory at the reactant state (a constant value accounting for the difference in absolute electronic energies), and the bracket $\langle ... \rangle_{\mathrm{LL}}$ indicates that the ensemble average is carried out using the potential $E^{\mathrm{LL}}_{\mathrm{tot}}$ (eq 2).

An important feature of eqs A1 and A2 is that one can obtain the *exact* DL-PMF with highly accurate treatment of the QM subsystem by running statistical samplings using the LL potential. If the structures sampled by the LL potential surface have a large overlap with that from HL calculations, the ensemble average for calculating $\Delta W^{\mathrm{HL}}(z)$ can be fast converging. However, in the present case, it is still a formidable task to enumerate the energies for the QM subsystem, which contains 109 atoms, at the B3LYP and MP2 levels of theory for the $E^{\mathrm{HL}}_{\mathrm{QM}}$ term in eq A2 "on the fly" during MD simulations. To circumvent this computational difficulty, we adopt the local harmonic approximation (*51*), in which the ensemble average of eq A2 is taken in a reference system where the difference between $E^{\mathrm{HL}}_{\mathrm{QM}}$ and $E^{\mathrm{LL}}_{\mathrm{QM}}$ harmonically oscillates about its minimum-energy reaction path (MEP) in the LL system with an angular frequency ω.

$$\langle \mathrm{e}^{-[E^{\mathrm{HL}}_{\mathrm{QM}}(z)-E^{\mathrm{LL}}_{\mathrm{QM}}(z)]/RT}\rangle_{\mathrm{LL}} \approx \langle \mathrm{e}^{-[E^{\mathrm{HL}}_{\mathrm{QM}}(z_\omega)-E^{\mathrm{LL}}_{\mathrm{QM}}(z_\omega)]/RT}\rangle_{\omega} \qquad \mathrm{(A3)}$$

where the coordinate z_ω refers configurations sampled by the harmonic approximation, and the ensemble average on the right-hand of the equation $\langle ... \rangle_\omega$ is over these configurations.

By Wick's rule (*109*), we can express the ensemble average as follows:

$$\Delta W^{\mathrm{HL}}_{\mathrm{QM}}(z) \approx \Delta \bar{E}^{\mathrm{HL}}(z_\omega) + \frac{1}{2RT}\langle[\Delta E^{\mathrm{HL}}(z_\omega) - \Delta \bar{E}^{\mathrm{HL}}(z_\omega)]^2\rangle_\omega \qquad \mathrm{(A4)}$$

where $\Delta E^{\mathrm{HL}}(z_\omega) = E^{\mathrm{HL}}_{\mathrm{QM}}(z_\omega) - E^{\mathrm{LL}}_{\mathrm{QM}}(z_\omega)$, and $\Delta \bar{E}^{\mathrm{HL}}(z_\omega) = \langle E^{\mathrm{HL}}_{\mathrm{QM}}(z_\omega) - E^{\mathrm{LL}}_{\mathrm{QM}}(z_\omega)\rangle_\omega$. Since the system harmonically oscillates about its MEP, $\Delta \bar{E}^{\mathrm{HL}}(z_\omega)$ equals $\Delta E^{\mathrm{HL}}(z^{\mathrm{MEP}}_{\mathrm{LL}})$

where $z_{\mathrm{LL}}^{\mathrm{MEP}}$ specifies the coordinates along the lower-level minimum energy path. If we omit the second order correction in eq A4, we obtain the following simple expression:

$$\Delta W_{\mathrm{QM}}^{\mathrm{HL}}(z) \approx \Delta E^{\mathrm{HL}}(z_{\mathrm{LL}}^{\mathrm{MEP}}) = E_{\mathrm{QM}}^{\mathrm{HL}}(z_{\mathrm{LL}}^{\mathrm{MEP}}) - E_{\mathrm{QM}}^{\mathrm{LL}}(z_{\mathrm{LL}}^{\mathrm{MEP}}) \quad \text{(A5)}$$

Therefore, the high-level correction to the lower-level potential of mean force only needs to be made by computing the potential energy difference between the HL and LL theory along the minimum energy path obtained from the latter potential. Note that the local harmonic approximation was made to estimate the correction term, whereas the free energy simulations are performed without any approximations.

SUPPORTING INFORMATION AVAILABLE

Comparison of structures and energies using the AM1, combined AM1:CHARMM22 potential, ab initio, or DFT methods in the dual-level calculations, and product−enzyme complex simulations along with information on an animation of the reaction pathway (12 pages). This material is available free of charge via the Internet at http://pubs.acs.org.

REFERENCES

1. Raushel, F. M. (2002) Bacterial detoxification of organophosphate nerve agents, *Curr. Opin. Microbiol. 5*, 288−295.
2. Kumar, S., Mukerji, K. G., and Lai, R. (1996) Molecular aspects of pesticide degradation by microorganisms, *Crit. Rev. Microbiol. 22*, 1−26.
3. Albuquerque, X. E., Pereira, E. F. R., Aracava, Y., Fawcett, W. P., Oliveira, M., Randall, W. R., Hamilton, T. A., Kan, R. K., Romano, J. A., Jr., and Adler, M. (2006) Effective countermeasure against poisoning by organophosphorus insecticides and nerve agents, *Proc. Natl. Acad. Sci. U.S.A. 103*, 13220−13225.
4. Omburo, G. A., Kuo, J. M., Mullins, L. S., and Raushel, F. M. (1992) Characterization of the zinc binding site of bacterial phosphotriesterase, *J. Biol. Chem. 267*, 13278−13283.
5. Caldwell, S. R., and Raushel, F. M. (1991) Detoxification of organophosphate pesticides using a nylon based immobilized phosphotriesterase from Pseudomonas diminuta, *Appl. Biochem. Biotechnol. 31*, 59−73.
6. Caldwell, S. R., and Raushel, F. M. (2006) Detoxification of organophosphate pesticides using an immobilized phosphotriesterase from *Pseudomonas diminuta*, *Biotechnol. Bioeng. 37*, 103−109.
7. Russell, A. J., Berberich, J. A., Drevon, G. F., and Koepsel, R. R. (2003) Biomaterials for mediation of chemical and biological warfare agents, *Annu. Rev. Biomed. Eng. 5*, 1−27.
8. Krauss, M., Olsen, L., Antony, J., and Hemmingsen, L. (2002) Coordination Geometries of Zn(II) and Cd(II) in Phosphotriesterase: Influence of Water Molecules in the Active Site, *J. Phys. Chem. B 106*, 9446−9453.
9. Krauss, M. (2001) Ab Initio Structure of the Active Site of Phosphotriesterase, *J. Chem. Inf. Model. 41*, 8−17.
10. Kafafi, S. A., and Krauss, M. (1999) Ab initio determination of the structure of the active site of a metalloenzyme: Metal substitution in phosphotriesterase using density functional methods, *Int. J. Quantum Chem. 75*, 289−299.
11. Koča, J., Zhan, C. G., Rittenhouse, R. C., and Ornstein, R. L. (2001) Mobility of the Active Site Bound Paraoxon and Sarin in Zinc-Phosphotriesterase by Molecular Dynamics Simulation and Quantum Chemical Calculation, *J. Am. Chem. Soc. 123*, 817−826.
12. Koča, J., Zhan, C.-G., Rittenhouse, R. C., and Ornstein, R. L. (2003) Coordination number of zinc ions in the phosphotriesterase active site by molecular dynamics and quantum mechanics, *J. Comput. Chem. 24*, 368−378.
13. Zhan, C. G., de Souza, O. N., Rittenhouse, R., and Ornstein, R. L. (1999) Determination of Two Structural Forms of Catalytic Bridging Ligand in Zinc-Phosphotriesterase by Molecular Dynamics Simulation and Quantum Chemical Calculation, *J. Am. Chem. Soc. 121*, 7279−7282.
14. Zheng, F., Zhan, C. G., and Ornstein, R. L. (2002) Theoretical Determination of Two Structural Forms of the Active Site in Cadmium-Containing Phosphotriesterases, *J. Phys. Chem. B 106*, 717−722.
15. Zheng, F., Zhan, C.-G., and Ornstein, R. L. (2001) Theoretical studies of reaction pathways and energy barriers for alkaline hydrolysis of phosphotriesterase substrates paraoxon and related toxic phosphofluoridate nerve agents, *J. Chem. Soc., Perkin Trans. 2*, 2355−2363.
16. Pang, Y.-P. (2001) Successful molecular dynamics simulation of two zinc complexes bridged by a hydroxide in phosphotriesterase using the cationic dummy atom method, *Proteins: Struct., Funct., Genet. 45*, 183−189.
17. Šečkute, J., Menke, J. L., Emnett, R. J., Patterson, E. V., and Cramer, C. J. (2005) Ab Initio Molecular Orbital and Density Functional Studies on the Solvolysis of Sarin and O,S-Dimethyl Methylphosphonothiolate, a VX-like Compound, *J. Org. Chem. 70*, 8649−8660.
18. Aubert, S. D., Li, Y., and Raushel, F. M. (2004) Mechanism for the Hydrolysis of Organophosphates by the Bacterial Phosphotriesterase, *Biochemistry 43*, 5707−5715.
19. Gao, J., Ma, S., Major, D. T., Nam, K., Pu, J., and Truhlar, D. G. (2006) Mechanisms and free energies of enzymatic reactions, *Chem. Rev. 106*, 3188−3209.
20. Gao, J. (1995) Methods and applications of combined quantum mechanical and molecular mechanical potentials, *Rev. Comput. Chem. 7*, 119−185.
21. Vanhooke, J. L., Benning, M. M., Raushel, F. M., and Holden, H. M. (1996) Three-Dimensional Structure of the Zinc-Containing Phosphotriesterase with the Bound Substrate Analog Diethyl 4-Methylbenzylphosphonate, *Biochemistry 35*, 6020−6025.
22. Benning, M. M., Hong, S.-B., Raushel, F. M., and Holden, H. M. (2000) The Binding of Substrate Analogs to Phosphotriesterase, *J. Biol. Chem. 275*, 30556−30560.
23. Wilcox, D. E. (1996) Binuclear metallohydrolases, *Chem. Rev. 96*, 2435−2458.
24. Mitić, N., Smith, S. J., Neves, A., Guddat, L. W., Gahan, L. R., and Schenk, G. (2006) The catalytic mechanisms of binuclear metallohydrolases, *Chem. Rev. 106*, 3338−3363.
25. Caldwell, S. R., Newcomb, J. R., Schlecht, K. A., and Raushel, F. M. (1991) Limits of diffusion in the hydrolysis of substrates by the phosphotriesterase from Pseudomonas diminuta, *Biochemistry 30*, 7438−7444.
26. Cleland, W. W., and Hengge, A. C. (2006) Enzymatic mechanisms of phosphate and sulfate transfer, *Chem. Rev. 106*, 3252−3278.
27. Hong, S. B., and Raushel, F. M. (1999) Stereochemical Constraints on the Substrate Specificity of Phosphotriesterase, *Biochemistry 38*, 1159−1165.
28. Chen-Goodspeed, M., Sogorb, M. A., Wu, F., Hong, S. B., and Raushel, F. M. (2001) Structural Determinants of the Substrate and Stereochemical Specificity of Phosphotriesterase, *Biochemistry 40*, 1325−1331.
29. Lewis, V. E., Donarski, W. J., Wild, J. R., and Raushel, F. M. (1988) Mechanism and stereochemical course at phosphorus of the reaction catalyzed by a bacterial phosphotriesterase, *Biochemistry 27*, 1591−1597.
30. Becke, A. D. (1988) Density-functional exchange-energy approximation with correct asymptotic behavior, *Phys. Rev. A 38*, 3098.
31. Lee, C., Yang, W., and Parr, R. G. (1988) Development of the Colle-Salvetti correlation-energy formula into a functional of the electron density, *Phys. Rev. B 37*, 785.
32. Stephens, P. J., Devlin, F. J., Chabalowski, C. F., and Frisch, M. J. (1994) Ab initio calculation of vibrational absorption and circular dichroism spectra using density functional force, *J. Phys. Chem. 98*, 11623.
33. Aqvist, J., and Warshel, A. (1993) Simulation of enzyme reactions using valence bond force fields and other hybrid quantum/classical approaches, *Chem. Rev. 93*, 2523−2544.
34. Field, M. J., Bash, P. A., and Karplus, M. (1990) A combined quantum mechanical and molecular mechanical potential for molecular dynamics simulations, *J. Comput. Chem. 11*, 700−733.
35. Gao, J., and Xia, X. (1992) A prior evaluation of aqueous polarization effects through Monte Carlo QM-MM simulations, *Science 258*, 631−635.
36. Mulholland, A. J. (2001) The QM/MM approach to enzymatic reactions, *Theor. Comput. Chem. 9*, 597−653.

37. Garcia-Viloca, M., Gao, J., Karplus, M., and Truhlar, D. G. (2004) How enzymes work: Analysis by modern rate theory and computer simulations, *Science 303*, 186−195.
38. Gao, J., and Truhlar, D. G. (2002) Quantum mechanical methods for enzyme kinetics, *Annu. Rev. Phys. Chem. 53*, 467−505.
39. Gao, J. (1993) Potential of mean force for the isomerization of DMF in aqueous solution: a Monte Carlo QM/MM simulation study, *J. Am. Chem. Soc. 115*, 2930−2935.
40. Gao, J. (1994) Origin of the solvent effects on the barrier to amide isomerization from combined QM/MM Monte Carlo simulations, *Proc.*−*Indian Acad. Sci., Chem. Sci. 106*, 507−519.
41. Byun, K., Mo, Y., and Gao, J. (2001) New Insight on the Origin of the Unusual Acidity of Meldrum's Acid from ab Initio and Combined QM/MM Simulation Study, *J. Am. Chem. Soc. 123*, 3974−3979.
42. Dewar, M. J. S., Zoebisch, E. G., Healy, E. F., and Stewart, J. P. (1985) AM1: A new general purpose quantum mechanical molecular model, *J. Am. Chem. Soc. 107*, 3902−3909.
43. Dewar, M. J. S., and Merz, K. M., Jr. (1988) AM1 parameters for zinc, *Organometallics 7*, 522−524.
44. Dewar, M. J. S., and Jie, C. (1989) AM1 parameters for phosphorus, *THEOCHEM 187*, 1−13.
45. Gao, J., Amara, P., Alhambra, C., and Field, M. J. (1998) A Generalized Hybrid Orbital (GHO) Method for the Treatment of Boundary Atoms in Combined QM/MM Calculations, *J. Phys. Chem. A 102*, 4714−4721.
46. Amara, P., Field, M. J., Alhambra, C., and Gao, J. (2000) The generalized hybrid orbital method for combined quantum mechanical/molecular mechanical calculations: formulation and tests of the analytical derivatives, *Theor. Chem. Acc. 104*, 336−343.
47. MacKerell, A. D., Jr., Bashford, D., Bellott, M., Dunbrack, R. L., Evanseck, J. D., Field, M. J., Fischer, S., Gao, J., Guo, H., Ha, S., Joseph-McCarthy, D., Kuchnir, L., Kuczera, K., Lau, F. T. K., Mattos, C., Michnick, S., Ngo, T., Nguyen, D. T., Prodhom, B., Reiher, W. E., III, Roux, B., Schlenkrich, M., Smith, J. C., Stote, R., Straub, J., Watanabe, M., Wiorkiewicz-Kuczera, J., Yin, D., and Karplus, M. (1998) All-Atom Empirical Potential for Molecular Modeling and Dynamics Studies of Proteins, *J. Phys. Chem. B 102*, 3586−3616.
48. Jorgensen, W. L., Chandrasekhar, J., Madura, J. D., Impey, R. W., and Klein, M. L. (1983) Comparison of simple potential functions for simulating liquid water, *J. Chem. Phys. 79*, 926−935.
49. Hehre, W. J., Radom, L., Schleyer, P. v. R., and Pople, J. A. (1986) *Ab initio molecular orbital theory*, Wiley, New York.
50. Parr, R. G., and Yang, W. (1989) *Density-functional theory of atoms and molecules*, Oxford University Press, Clarendon Press, New York, NY, Oxford, U.K.
51. Friesner, R. A., and Guallar, V. (2005) Ab initio quantum chemical and mixed quantum mechanics/molecular mechanics (QM/MM) methods for studying enzymatic catalysis, *Annu. Rev. Phys. Chem. 56*, 389−427.
52. Carloni, P., and Rothlisberger, U. (2001) Simulations of enzymatic systems: Perspectives from Car-Parrinello molecular dynamics simulations, *Theor. Comput. Chem. 9*, 215−251.
53. Stewart, J. J. P. (1990) MOPAC: a semiempirical molecular orbital program, *J. Comput.-Aided Mol. Des. 4*, 1−105.
54. Cui, Q., Elstner, M., Kaxiras, E., Frauenheim, T., and Karplus, M. (2001) *J. Phys. Chem. B 105*, 569.
55. Bhattacharyya, S., Ma, S., Stankovich, M. T., Truhlar, D. G., and Gao, J. (2005) Potential of Mean Force Calculation for the Proton and Hydride Transfer Reactions Catalyzed by Medium-Chain Acyl-CoA Dehydrogenase: Effect of Mutations on Enzyme Catalysis, *Biochemistry 44*, 16549−16562.
56. Brothers, E. N., Suarez, D., Deerfield, D. W., II, and Merz, K. M., Jr. (2004) PM3-compatible zinc parameters optimized for metalloenzyme active sites, *J. Comput. Chem. 25*, 1677−1692.
57. (a) Nam, K., Cui, Q., Gao, J., and York, D. M. (2007) A specific reaction parameterization of the AM1/d Hamiltonian for phosphoryl transfer reactions, *J. Chem. Theory Comput. 3*, 486−504. (b) Lopez, X., and York, D. M. (2003) Parameterization of semiempirical methods to treat nucleophilic attacks to biological phosphates: AM1/d parameters for phosphorus, *Theor. Chem. Acc. 109*, 149−159.
58. Corchado, J. C., and Truhlar, D. G. (1998) Dual-level methods for electronic structure calculations of potential energy functions that use quantum mechanics as the lower level, in *Combined Quantum Mechanical and Molecular Mechanical Methods* (Gao, J., and Thompson, M. A., Eds.) pp 106−127, American Chemical Society, Wahsington, DC.
59. Proust-De Martin, F., Dumas, R., and Field, M. J. (2000) A Hybrid-Potential Free-Energy Study of the Isomerization Step of the Acetohydroxy Acid Isomeroreductase Reaction, *J. Am. Chem. Soc. 122*, 7688−7697.
60. Marti, S., Moliner, V., Tunon, I., and Williams, I. H. (2005) Computing Kinetic Isotope Effects for Chorismate Mutase with High Accuracy. A New DFT/MM Strategy, *J. Phys. Chem. B 109*, 3707−3710.
61. Marti, S., Moliner, V., and Tunon, I. (2005) Improving the QM/MM Description of Chemical Processes: A Dual Level Strategy To Explore the Potential Energy Surface in Very Large Systems, *J. Chem. Theory Comput. 1*, 1008−1016.
62. Ferrer, S., Ruiz-Pernia, J. J., Tunon, I., Moliner, V., Garcia-Viloca, M., Gonzalez-Lafont, A., and Lluch, J. M. (2005) A QM/MM Exploration of the Potential Energy Surface of Pyruvate to Lactate Transformation Catalyzed by LDH. Improving the Accuracy of Semiempirical Descriptions, *J. Chem. Theory Comput. 1*, 750−761.
63. Rod, T. H., and Ryde, U. (2005) Accurate QM/MM Free Energy Calculations of Enzyme Reactions: Methylation by Catechol O-Methyltransferase, *J. Chem. Theory Comput. 1*, 1240−1251.
64. Svensson, M., Humbel, S., Froese, R. D. J., Matsubara, T., Sieber, S., and Morokuma, K. (1996) ONIOM: A Multi-Layered Integrated MO + MM Method for Geometry Optimizations and Single Point Energy Predictions. A Test for Diels-Alder Reactions and Pt(P(t-Bu)3)2 + H2 Oxidative Addition, *J. Phys. Chem. 100*, 19357−19363.
65. Bakowies, D., and Thiel, W. (1996) Hybrid Models for Combined Quantum Mechanical and Molecular Mechanical Approaches, *J. Phys. Chem. 100*, 10580−10594.
66. Garcia-Viloca, M., Truhlar Donald, G., and Gao, J. (2003) Importance of substrate and cofactor polarization in the active site of dihydrofolate reductase, *J. Mol. Biol. 327*, 549−560.
67. Orozco, M., Luque, F. J., Habibollahzadeh, D., and Gao, J. (1995) The polarization contribution to the free energy of hydration, *J. Chem. Phys. 102, 6145−6152.* Erratum, *J. Chem. Phys. 103*, 9112.
68. Gao, J. (1996) Hybrid Quantum Mechanical/Molecular Mechanical Simulations: An Alternative Avenue to Solvent Effects in Organic Chemistry, *Acc. Chem. Res. 29*, 298−305.
69. Gao, J. (1995) An Automated Procedure for Simulating Chemical Reactions in Solution. Application to the Decarboxylation of 3-Carboxybenzisoxazole in Water, *J. Am. Chem. Soc. 117*, 8600−8607.
70. Mo, Y., and Gao, J. (2000) Ab initio QM/MM simulations with a molecular orbital-valence bond (MOVB) method: application to an SN2 reaction in water, *J. Comput. Chem. 21*, 1458−1469.
71. Gao, J., and Byun, K. (1997) Solvent effects on the $n \rightarrow \pi^*$ transition of pyrimidine in aqueous solution, *Theor. Chem. Acc. 96*, 151−156.
72. Easton, R. E., Giesen, D. J., Welch, A., Cramer, C. J., and Truhlar, D. G. (1996) The MIDI! basis set for quantum mechanical calculations of molecular geometries and partial charges, *Theor. Chim. Acta 93*, 281−301.
73. Frisch, M. J., Trucks, G. W., Schlegel, H. B., Scuseria, G. E., Robb, M. A., Cheeseman, J. R., Montgomery, J. A., Jr., Vreven, T., Kudin, K. N., Burant, J. C., Millam, J. M., Iyengar, S. S., Tomasi, J., Barone, V., Mennucci, B., Cossi, M., Scalmani, G., Rega, N., Petersson, G. A., Nakatsuji, H., Hada, M., Ehara, M., Toyota, K., Fukuda, R., Hasegawa, J., Ishida, M., Nakajima, T., Honda, Y., Kitao, O., Nakai, H., Klene, M., Li, X., Knox, J. E., Hratchian, H. P., Cross, J. B., Bakken, V., Adamo, C., Jaramillo, J., Gomperts, R., Stratmann, R. E., Yazyev, O., Austin, A. J., Cammi, R., Pomelli, C., Ochterski, J. W., Ayala, P. Y., Morokuma, K., Voth, G. A., Salvador, P., Dannenberg, J. J., Zakrzewski, V. G., Dapprich, S., Daniels, A. D., Strain, M. C., Farkas, O., Malick, D. K., Rabuck, A. D., Raghavachari, K., Foresman, J. B., Ortiz, J. V., Cui, Q., Baboul, A. G., Clifford, S., Cioslowski, J., Stefanov, B. B., Liu, G., Liashenko, A., Piskorz, P., Komaromi, I., Martin, R. L., Fox, D. J., Keith, T., Al-Laham, M. A., Peng, C. Y., Nanayakkara, A., Challacombe, M., Gill, P. M. W., Johnson, B., Chen, W., Wong, M. W., Gonzalez, C., and Pople, J. A. (2004) *Gaussian 03*, revision C.02, Gaussian, Inc., Wallingford, CT.
74. Brooks, B. R., Bruccoleri, R. E., Olafson, B. D., States, D. J., Swaminathan, S., and Karplus, M. (1983) CHARMM: a program for macromolecular energy, minimization, and dynamics calculations, *J. Comput. Chem. 4*, 187−217.

75. Johnston, H. S. (1966) *Gas phase reaction rate theory*, Ronald Press Co., New York.
76. Kirkwood, J. G. (1935) Statistical mechanics of fluid mixtures, *J. Chem. Phys. 3*, 300−313.
77. Villa, J., and Warshel, A. (2001) Energetics and dynamics of enzymatic reactions, *J. Phys. Chem. B 105*, 7887−7907.
78. Torrie, G. M., and Valleau, J. P. (1977) Nonphysical sampling distributions in Monte Carlo free-energy estimation: Umbrella sampling, *J. Comput. Phys. 23*, 187−199.
79. Kumar, S., Bouzida, D., Swendsen, R. H., Kollman, P. A., and Rosenberg, J. M. (1992) The weighted histogram analysis method for free-energy calculations on biomolecules. I. The method, *J. Comput. Chem. 13*, 1011−1021.
80. Alhambra, C., Corchado, J., Sanchez, M. L., Garcia-Viloca, M., Gao, J., and Truhlar, D. G. (2001) Canonical Variational Theory for Enzyme Kinetics with the Protein Mean Force and Multidimensional Quantum Mechanical Tunneling Dynamics. Theory and Application to Liver Alcohol Dehydrogenase, *J. Phys. Chem. B 105*, 11326−11340.
81. Brooks, C. L., III, Brunger, A., and Karplus, M. (1985) Active site dynamics in protein molecules: a stochastic boundary molecular-dynamics approach, *Biopolymers 24*, 843−865.
82. Brooks, C. L., III., and Karplus, M. (1989) Solvent effects on protein motion and protein effects on solvent motion. Dynamics of the active site region of lysozyme, *J. Mol. Biol. 208*, 159−181.
83. Brooks, C. L., III, and Karplus, M. (1983) Deformable stochastic boundaries in molecular dynamics, *J. Chem. Phys. 79*, 6312−6325.
84. Ryckaert, J. P., Ciccotti, G., and Berendsen, H. J. C. (1977) Numerical integration of the Cartesian equations of motion of a system with constraints: molecular dynamics of n-alkanes, *J. Comput. Phys. 23*, 327−341.
85. Verlet, L. (1967) Computer "experiments" on classical fluids. I. Thermodynamical properties of Lennard-Jones molecules, *Phys. Rev. 159*, 98−103.
86. Alhambra, C., and Gao, J. (2000) Hydrogen-bonding interactions in the active site of a low molecular weight protein-tyrosine phosphatase, *J. Comput. Chem. 21*, 1192−1203.
87. Garcia-Viloca, M., Alhambra, C., Truhlar, D. G., and Gao, J. (2002) Quantum dynamics of hydride transfer catalyzed by bimetallic electrophilic catalysis: synchronous motion of Mg^{2+} and H- in xylose isomerase, *J. Am. Chem. Soc. 124*, 7268−7269.
88. Garcia-Viloca, M., Alhambra, C., Truhlar Donald, G., and Gao, J. (2003) Hydride transfer catalyzed by xylose isomerase: mechanism and quantum effects, *J. Comput. Chem. 24*, 177−190.
89. Humphrey, W., Dalke, A., and Schulten, K. (1996) VMD: visual molecular dynamics, *J. Mol. Graphics 14*, 33−38.
90. Dennington, R., II, Keith, T., Millam, J., Eppinnett, K., Hovell, W. L., and Gilliland, R. (2003) *GaussView*, version 3.07, Semichem, Inc., Shawnee Mission, KS.
91. Hammond, G. S. (1955) A correlation of reaction rates, *J. Am. Chem. Soc. 77*, 334−338.
92. Curtiss, L. A., Raghavachari, K., Redfern, P. C., Rassolov, V., and Pople, J. A. (1998) Gaussian-3 (G3) theory for molecules containing first and second-row atoms, *J. Chem. Phys. 109*, 7764−7776.
93. Baker, J., Muir, M., and Andzelm, J. (1995) A study of some organic reactions using density functional theory, *J. Chem. Phys. 102*, 2063−2079.
94. Lynch, B. J., and Truhlar, D. G. (2001) How Well Can Hybrid Density Functional Methods Predict Transition State Geometries and Barrier Heights?, *J. Phys. Chem. A 105*, 2936−2941.
95. Thoden, J. B., Phillips, G. N., Jr., Neal, T. M., Raushel, F. M., and Holden, H. M. (2001) Molecular structure of dihydroorotase: a paradigm for catalysis through the use of a binuclear metal center, *Biochemistry 40*, 6989−6997.
96. Lavie, A., Allen, K. N., Petsko, G. A., and Ringe, D. (1994) X-ray Crystallographic Structures of D-Xylose Isomerase-Substrate Complexes Position the Substrate and Provide Evidence for Metal Movement during Catalysis, *Biochemistry 33*, 5469−5480.
97. Allen, K. N., Lavie, A., Petsko, G. A., and Ringe, D. (1995) Design, Synthesis, and Characterization of a Potent Xylose Isomerase Inhibitor, D-Threonohydroxamic Acid, and High-Resolution X-ray Crystallographic Structure of the Enzyme-Inhibitor Complex, *Biochemistry 34*, 3742−3749.
98. Chen, S.-L., Fang, W.-H., Himo, F. (2007) Theoretical Study of the Phosphotriesterase Reaction Mechanism, *J. Phys. Chem. B 111*, 1253.
99. Garcia-Viloca, M., Truhlar, D. G., and Gao, J. (2003) Reaction-Path Energetics and Kinetics of the Hydride Transfer Reaction Catalyzed by Dihydrofolate Reductase, *Biochemistry 42*, 13558−13575.
100. Chandrasekhar, J., and Jorgensen, W. L. (1985) Energy profile for a nonconcerted SN2 reaction in solution, *J. Am. Chem. Soc. 107*, 2974−2975.
101. Liu, Y., Gregersen, B. A., Hengge, A., and York, D. M. (2006) Transesterification Thio Effects of Phosphate Diesters: Free Energy Barriers and Kinetic and Equilibrium Isotope Effects from Density-Functional Theory, *Biochemistry 45*, 10043−10053.
102. Silverman, D. N., and Lindskog, S. (1988) *Acc. Chem. Res. 21*, 30.
103. Jackson, C., Kim, H. K., Carr, P. D., Liu, J. W., and Ollis, D. L. (2005) The Structure of an Enzyme-Product Complex Reveals the Critical Role of a Terminal Hydroxide Nucleophile in the Bacterial Phosphotriesterase Mechanism, *Biochim. Biophys. Acta 1752*, 56.
104. Benini, S., Rypniewski, W. R., Wilson, K. S., Ciurli, S., and Mangani, S. (1999) A New Proposal for Urease Mechanism Based on the Crystal Structures of the Native and Inhibited Enzyme From Bacillus Pasteurii: Why Urea hydrolysis Costs two Nickels, *Struct. Fold. Des. 7*, 205.
105. Thoden, J. B., Marti-Arbona, R., Raushel, F. M., and Holden, H. M. (2003) High Resolution X-ray Structure of Isoaspartyl Dipeptidase from Escherichia Coli, *Biochemistry 42*, 4874.
106. Whiltlow, M., Howard, A. J., Finzel, B. C., Poulos, T. L., Winborne, E., and Gilliland, G. L. (1991) A Metal-Mediated Hydride Shift Mechanism for Xylose Isomerase based on the 1.6 A Streptomyces Rubiginosus Structure with Xylitol and D-Xylose, *Proteins: Struct., Funct., Genet. 9*, 153−173.
107. Gao, J., Byun, K. L., and Kluger, R. (2004) Catalysis by Enzyme Conformational Change, *Top. Curr. Chem. 238*, 113−136.
108. Garcia-Viloca, M., Poulsen, T. D., Truhlar, D. G., and Gao, J. (2004) Sensitivity of Molecular Dynamics Simulations to the Choice of the X-Ray Structure used to Model an Enzymatic Reaction, *Protein Sci. 13*, 2341−2354.
109. Kleinert, H. (2004) *Path integrals in quantum mechanics, statistics, polymer physics, and financial markets*, 3rd ed., World Scientific, Singapore, River Edge, NJ.

BI700460C